Weierstraß-Institut
für Angewandte Analysis und Stochastik

Leibniz-Institut im Forschungsverbund Berlin e. V.

Preprint ISSN 2198-5855

Multi-dimensional modeling and simulation of semiconductor nanophotonic devices

Markus Kantner[1], Theresa Höhne[2], Thomas Koprucki[1], Sven Burger[2],

Hans-Jürgen Wünsche[1,3], Frank Schmidt[2], Alexander Mielke[1,4], Uwe Bandelow[1]

submitted: December 3, 2019

[1] Weierstraß-Institut
Mohrenstr. 39
10117 Berlin
Germany
E-Mail: markus.kantner@wias-berlin.de
thomas.koprucki@wias-berlin.de
hans-juergen.wuensche@wias-berlin.de
alexander.mielke@wias-berlin.de
uwe.bandelow@wias-berlin.de

[2] Zuse-Institut Berlin
Takustr. 7
14195 Berlin
Germany
E-Mail: hoehne@zib.de
burger@zib.de
frank.schmidt@zib.de

[3] Ferdinand-Braun-Institut
Leibniz-Institut für Höchstfrequenztechnik
Gustav-Kirchhoff-Str. 4
12489 Berlin
Germany

[4] Institut für Mathematik
Humboldt-Universität zu Berlin
Unter den Linden 6
10099 Berlin
Germany

No. 2653
Berlin 2019

2010 *Physics and Astronomy Classification Scheme.* 02.70.Dh, 03.50.De, 42.50.-p, 42.55.Px, 47.11.Df, 81.07.Ta, 85.60.-q.

Key words and phrases. Nanophotonic devices, device simulation, multi-physics models, VCSELs, single-photon sources, waveguides, quantum dots, van Roosbroeck system, drift-diffusion equations, Maxwell equations, Lindblad master equation, GENERIC, optical resonance modes, degenerate semiconductors, finite volume method, finite element method.

This work has been supported by the German Research Foundation (DFG) within the collaborative research center SFB 787 *Semiconductor Nanophotonics* under grant B4. The authors would like to thank Patricio Farrell, Jürgen Fuhrmann, Philipp Gutsche, Jan Pomplun, Nella Rotundo, Alexander Wilms, Benjamin Wohlfeil and Lin Zschiedrich for excellent collaboration and valuable discussions.

Edited by
Weierstraß-Institut für Angewandte Analysis und Stochastik (WIAS)
Leibniz-Institut im Forschungsverbund Berlin e. V.
Mohrenstraße 39
10117 Berlin
Germany

Fax: +49 30 20372-303
E-Mail: preprint@wias-berlin.de
World Wide Web: http://www.wias-berlin.de/

Multi-dimensional modeling and simulation of semiconductor nanophotonic devices

Markus Kantner, Theresa Höhne, Thomas Koprucki, Sven Burger,
Hans-Jürgen Wünsche, Frank Schmidt, Alexander Mielke, Uwe Bandelow

Abstract

Self-consistent modeling and multi-dimensional simulation of semiconductor nanophotonic devices is an important tool in the development of future integrated light sources and quantum devices. Simulations can guide important technological decisions by revealing performance bottlenecks in new device concepts, contribute to their understanding and help to theoretically explore their optimization potential. The efficient implementation of multi-dimensional numerical simulations for computer-aided design tasks requires sophisticated numerical methods and modeling techniques. We review recent advances in device-scale modeling of quantum dot based single-photon sources and laser diodes by self-consistently coupling the optical Maxwell equations with semi-classical carrier transport models using semi-classical and fully quantum mechanical descriptions of the optically active region, respectively. For the simulation of realistic devices with complex, multi-dimensional geometries, we have developed a novel hp-adaptive finite element approach for the optical Maxwell equations, using mixed meshes adapted to the multi-scale properties of the photonic structures. For electrically driven devices, we introduced novel discretization and parameter-embedding techniques to solve the drift-diffusion system for strongly degenerate semiconductors at cryogenic temperature. Our methodical advances are demonstrated on various applications, including vertical-cavity surface-emitting lasers, grating couplers and single-photon sources.

1 Introduction

Nanophotonic devices based on semiconductor nanostructures embedded in optical micro-resonators enable a broad range of applications, including optical telecommunication and signal processing, photovoltaics, optical interconnects, medical imaging and sensing [1–5]. The optimal design of novel devices tailored to specific applications is a considerable challenge, that can be assisted by mathematical modeling and multi-dimensional numerical simulations. This requires efficient multi-physics TCAD (technology computer-aided design) simulation tools, which allow for the calculation of electromagnetic fields in photonic resonators, the electronic structure of semiconductor materials, the carrier transport dynamics in complex device geometries and the interaction of light with electron-hole excitations in the optically active nanostructures. TCAD simulation tools enable detailed studies of the complex interplay of various processes in opto-electronic devices on different time and length scales. Numerical simulations can provide information that are difficult to access experimentally, help to reveal performance bottlenecks, reduce the development costs of new prototypes, and allow to assess the optimization potential of particular design adaptations.

This chapter provides a survey on modeling fundamentals, recent advances in numerical methods and several example applications. Basic concepts of semi-classical carrier transport theory and optical field calculations are reviewed in Sec. 2. In Sec. 3, the focus lies on coupled opto-electronic modeling of

DOI 10.20347/WIAS.PREPRINT.2653 Berlin 2019

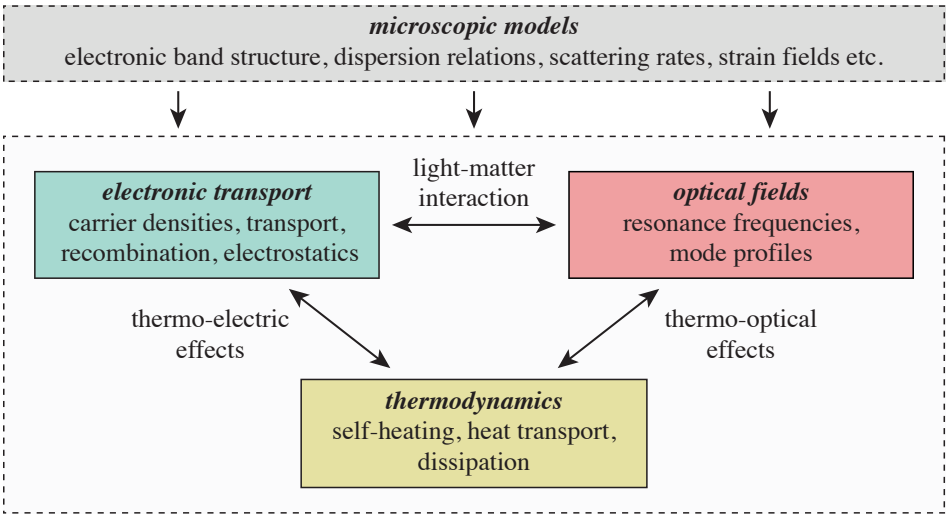

Fig. 1. Modeling of semiconductor opto-electronic devices is a multi-physics problem that requires the self-consistent coupling of physical models for the transport of charge carriers, optical fields and heating effects.

specific nanophotonic devices with quantum dot (QD) active regions. Here we outline a rate equation based semi-classical QD laser model (Sec. 3.1) and a hybrid quantum-classical modeling approach developed for QD-based single-photon emitting diodes (Sec. 3.2). Section 4 provides a review of several recent advances in the development of numerical methods for the drift-diffusion system and Maxwell's equations. In particular, we highlight new discretization and path following schemes for strongly degenerate semiconductors at cryogenic operation temperatures and mixed finite element methods for the vectorial Maxwell's equations with controlled high accuracy beyond the limits of standard tools. The newly developed numerical methods and modeling approaches are demonstrated with selected example applications in Sec. 5, including QD-based single-photon sources (Secs. 5.1, 5.4), vertical-cavity surface-emitting lasers (Sec. 5.2) and grating couplers (Sec. 5.3).

2 Basic concepts

The mathematical modeling of semiconductor opto-electronic devices is a multi-physics problem, that requires the self-consistent solution of several different physical models, see Fig. 1. The key problems are the description of the charge transport in semiconductor devices and the calculation of optical fields in photonic resonators, which will be reviewed in Secs. 2.1 and 2.2, respectively. These two "building blocks" are coupled by appropriate models for the light-matter interaction in the optically active region. As the spatial and temporal scales involved in the problem vary drastically between different devices (e.g., large-scale broad area lasers, miniaturized nanolasers or single-photon emitting diodes), there is no general model for the description of the active region of opto-electronic devices. Hence, one has to resort to approximations that are tailored to the characteristics of the particular device at hand. Moreover, in the field of modeling of nanophotonic devices, one distinguishes between a semi-classical theory (quantization of matter, classical optical fields) for conventional semiconductor lasers and a fully quantum mechanical theory in quantum optical devices. In Sec. 3, the opto-electronic coupling is presented in detail for vertical-emitting QD lasers (Sec. 3.1) and a QD-based single-photon emitting diode (Sec. 3.2). As self-heating and other thermal effects often play a significant role in opto-electronic devices [6–9], the generation and transport of heat is considered as a further building block. The fully coupled thermo-opto-electronic problem allows for the description of various thermo-electric and thermo-optical coupling effects. The consistent coupling of the physical models as sketched in Fig. 1

is a non-trivial task and requires particular attention to guarantee important conservation laws and consistency with fundamental thermodynamic principles.

The macroscopic models for charge and heat transport as well as the models for the optical fields involve several material parameters and phenomenological relations, that need to be provided by either experimental data or pre-computed microscopic calculations. This comprises, e.g., the electronic band structure, carrier scattering rates, strain fields and optical dispersion relations. As above, there is no general approach and the particularities depend on the device of interest. If certain microscopic degrees of freedom strongly interact with the macroscopic variables, they can not be regarded as fixed background parameters and need to be included as dynamically changing variables in the self-consistently coupled model.

2.1 Electronic transport

The transport of charge carriers in semiconductor devices is described by the van Roosbroeck system [10, 11], which is a system of three nonlinearly coupled partial differential equations on the computational domain $\Omega \in \mathbb{R}^d$, $d \in \{1, 2, 3\}$ that reads

$$-\nabla \cdot \varepsilon \nabla \phi = q\left(C + p - n\right), \tag{1a}$$

$$\partial_t n - \frac{1}{q}\nabla \cdot \mathbf{j}_n = -R, \tag{1b}$$

$$\partial_t p + \frac{1}{q}\nabla \cdot \mathbf{j}_p = -R. \tag{1c}$$

The electrostatic interaction between the carriers is described by Poisson's Eq. (1a), that determines the electrostatic potential ϕ generated by the (net-)charge density $q\left(C + p - n\right)$. Here, q denotes the elementary charge, n is the density of electrons, p is the density of holes and $C = N_D^+ - N_A^-$ is the built-in doping profile. The dielectric constant $\varepsilon = \varepsilon_0 \varepsilon_s$ is given by the vacuum permittivity ε_0 and the relative permittivity of the material ε_s in the static limit. The continuity Eqs. (1b)–(1c) describe the transport and recombination dynamics of the electrons and holes, respectively, where $\mathbf{j}_{n/p}$ are the charge current densities and R is the (net-)recombination rate.

2.1.1 Carrier densities, current densities and degeneration effects

Due to fast intraband scattering processes, the carrier densities in each band thermalize on a very short time scale such that they can be described by *quasi-equilibrium* distribution functions. The carrier densities are given via the state equations

$$n = N_c \mathscr{F}\left(\frac{\mu_c + q\phi - E_c}{k_B T}\right), \qquad p = N_v \mathscr{F}\left(\frac{E_v - q\phi - \mu_v}{k_B T}\right), \tag{2}$$

where the quasi-Fermi energies μ_c and μ_v describe the filling of the respective bands. Here, E_c and E_v denote the conduction and the valence band edge energy, T is the absolute temperature and k_B is Boltzmann's constant. The conduction band and valence band effective density of states N_c and N_v as well as the function $\mathscr{F}$ depend on the electronic density of states and the statistical distribution function. Assuming Fermi–Dirac statistics and parabolic energy bands (effective mass approximation), the function $\mathscr{F}$ is given by the Fermi–Dirac integral

$$\mathscr{F}\left(\eta\right) = F_\nu\left(\eta\right) = \frac{1}{\Gamma\left(\nu + 1\right)} \int_0^\infty \mathrm{d}\zeta \, \frac{\zeta^\nu}{\exp\left(\zeta - \eta\right) + 1}, \tag{3}$$

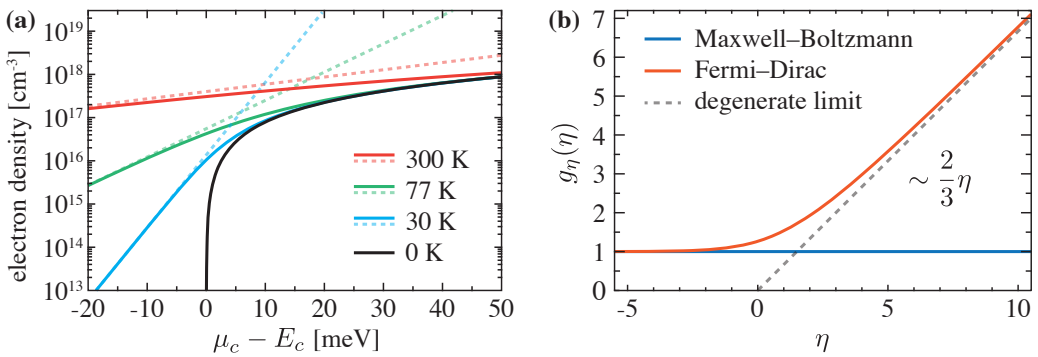

Fig. 2. (a) Electron density in GaAs as a function of the quasi-Fermi energy μ_c for different temperatures. The carrier density calculated using the Fermi–Dirac integral (solid lines) is compared with the Maxwell–Boltzmann approximation (dashed lines). **(b)** Plot of the degeneracy factor $g_\eta(\eta) = g(\mathscr{F}(\eta))$ according to Eq. (6), which leads to an enhancement of the diffusion current. Reprinted, with permission, from Ref. [12]. © 2016 Springer Science+Business Media.

where, e.g., $\nu = 1/2$ in 3D bulk materials or $\nu = 0$ in 2D systems (quantum wells). In the low density limit (i.e., $\eta < -1$), degeneration effects due to Fermi–Dirac statistics are negligible such that $\mathscr{F}(\eta) \approx \exp(\eta)$, see Fig. 2. This corresponds to the classical Maxwell–Boltzmann distribution in kinetic gas theory.

The current densities are driven by the gradients of the quasi-Fermi energies

$$\mathbf{j}_n = M_n n \nabla \mu_c, \qquad \mathbf{j}_p = M_p p \nabla \mu_v, \tag{4a}$$

where M_n and M_p are the respective carrier mobilities. In the thermodynamic equilibrium, the quasi-Fermi energies become a common global constant $\mu_{\text{eq}} = \text{const.}$, such that the (net-)current flux is zero. Using the carrier density relations (2), the current densities can be cast in the drift-diffusion form

$$\mathbf{j}_n = -qM_n n \nabla \phi + qD_n(n) \nabla n, \qquad \mathbf{j}_p = -qM_p p \nabla \phi - qD_p(p) \nabla p, \tag{4b}$$

where the diffusion coefficients $D_{n/p}$ are connected with the carrier mobilities via the *generalized* Einstein relations

$$D_n(n) = \frac{k_B T M_n}{q} g\left(\frac{n}{N_c}\right), \qquad D_p(p) = \frac{k_B T M_p}{q} g\left(\frac{p}{N_v}\right). \tag{5}$$

The expressions (5) feature the carrier density-dependent *degeneracy factor*

$$g(x) = x(\mathscr{F}^{-1})'(x), \tag{6}$$

which describes a nonlinear enhancement (because of $g(x) \geq 1$) of the diffusion current in the case of degenerate carrier statistics. For $\mathscr{F}(\eta) = \exp(\eta)$, one recovers the classical result $g \equiv 1$ corresponding to linear diffusion.

2.1.2 Recombination rate models

The (net-)recombination rate R in Eqs. (1b)–(1c) describes various radiative and non-radiative recombination and generation processes that lead to the annihilation or creation of electron-hole pairs. The dominant processes in opto-electronic semiconductor devices are illustrated in Fig. 3. For Shockley–Read–Hall recombination, spontaneous radiative recombination and Auger recombination (see Fig. 3 (a)–(c)), the recombination rate takes the form [13]

$$R = \left(1 - \exp\left(-\frac{\mu_c - \mu_v}{k_B T}\right)\right) \sum_\alpha r_\alpha(\mu_c, \mu_v, \phi), \tag{7}$$

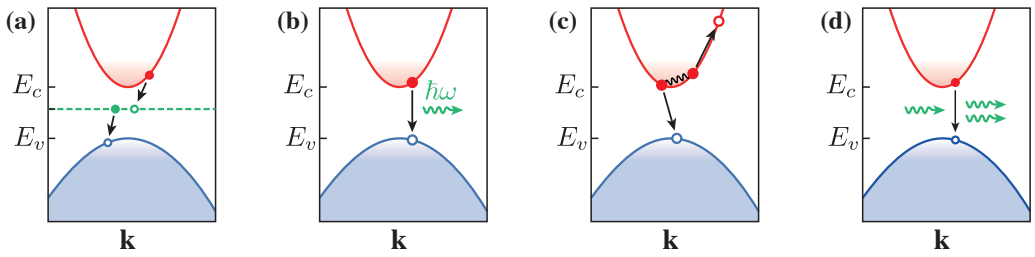

Fig. 3. Recombination processes in opto-electronic semiconductor devices: **(a)** Shockley–Read–Hall recombination of an electron-hole pair via relaxation to an intermediate trap state within the band gap, **(b)** spontaneous radiative recombination, **(c)** Auger recombination via an additional intraband scattering process and **(d)** stimulated recombination. The picture is taken from Ref. [13].

where α labels the various processes and r_α are process specific (non-negative) recombination rates, that are derived from quantum mechanical perturbation theory (i.e., Fermi's golden rule) [14, 15]. The first factor in Eq. (7) controls the ratio between carrier generation and recombination and vanishes under thermodynamic equilibrium conditions $\mu_c \equiv \mu_v \equiv \mu_{\text{eq}}$. This reflects the detailed balance condition due to the microscopic reversibility of the underlying kinetic equations. For details on the recombination rate models r_α we refer to Refs. [11, 16, 17]. Note that the stimulated recombination rate, see Fig. 3 (d), is not of type (7), as it depends also on the photon number in the laser mode. We will come back to this in Sec. 3.1.

2.1.3 Boundary conditions

The van Roosbroeck system (1) must be supplemented with boundary conditions modeling electrical contacts (Ohmic contacts, Schottky contacts, gate contacts), semiconductor-insulator interfaces or artificial boundaries of the computational domain $\partial\Omega$. These are typically mixed conditions on disjoint parts of the boundary given by either Neumann, Dirichlet or Robin boundary conditions. A generic approach that is very useful for the implementation in numerical software tools are Robin boundary conditions (boundary conditions of third kind)

$$\mathbf{n} \cdot \nabla u + \alpha_u \left(u - u_0\right) = 0, \tag{8}$$

where $u \in (\phi, \mu_c, \mu_v)$ is any of the basic variables, and $\mathbf{n}$ is the outward-oriented normal vector on $\partial\Omega$. The condition (8) is a weighted combination of homogeneous Neumann boundary conditions ($\alpha_u \to 0$: $\mathbf{n} \cdot \nabla u = 0$) and Dirichlet boundary conditions ($|\alpha_u| \to \infty$: $u = u_0$). For details on specific boundary condition models we refer to Refs. [11, 17, 18]. of this book

2.2 Optical fields

Optical processes in photonic devices are mathematically described by Maxwell's equations in terms of electric fields $\mathbf{E}(\mathbf{r}, t)$ and magnetic fields $\mathbf{H}(\mathbf{r}, t)$ in space $\mathbf{r}$ and time t. We briefly sketch the models used in photonics, more detailed information can be found, e.g., in Ref. [19].

Here, we are interested in solutions for specific frequencies ω, therefore the time dependency of the real electric field $\mathbf{E}(\mathbf{r}, t)$ is expressed by means of the complex electric field $\underline{\mathbf{E}}$ with $\mathbf{E}(\mathbf{r}, t) = \mathrm{Re}\left(\underline{\mathbf{E}} \exp\left(-i\omega t\right)\right)$. Since all field quantities are expressed in this way, the underline character is dropped and all fields and current densities are complex vectors. In its simplest form, i.e., when the entire electromagnetic field is generated by an impressed current density $\mathbf{J}_{\text{source}}$ of frequency ω,

Maxwell's equations yield

$$\nabla \times \mu(\mathbf{r})^{-1} \nabla \times \mathbf{E}(\mathbf{r}) - \omega^2 \varepsilon(\mathbf{r}) \mathbf{E}(\mathbf{r}) = i\omega \mathbf{J}_{\text{source}}(\mathbf{r}). \tag{9}$$

In Eq. (9) we identify the material properties as permittivity $\varepsilon = \varepsilon_r \varepsilon_0$ and permeability $\mu = \mu_r \mu_0$, where $\varepsilon_0 (\mu_0)$ and $\varepsilon_r (\mu_r)$ are the free space and relative permittivities (permeabilities). For all relevant optical materials, the relative permeability is $\mu_r = 1$, and the refractive index n is given by $n = \sqrt{\varepsilon_r}$. For the applications discussed in this chapter, Eq. (9) is enhanced to cover three different settings: (i) light scattering simulations, where external source fields $\mathbf{E}_{\text{source}}$ are present, (ii) resonance mode computations, for investigation of the modal structure of the setup, and (iii) propagation mode computation for investigation of waveguide structures. To cope with these situations, Maxwell's equations are used in properly adapted forms.

In *scattering problems on unbounded domains* a source field $\mathbf{E}_{\text{source}}$ is given which travels through (unbounded) space, being itself a solution to Maxwell's equations. Without a scattering object this would be the only field, i.e., the total field $\mathbf{E} = \mathbf{E}_{\text{source}}$. But if it hits an object, a scattered field $\mathbf{E}_{\text{scatt}}$ is generated. We compute the field $\mathbf{E} = \mathbf{E}_{\text{source}} + \mathbf{E}_{\text{scatt}}$ inside a computational domain Ω which we also call the interior domain, in contrast to the exterior domain Ω_{ext} surrounding Ω. Further we denote the boundary of the computational domain with $\partial\Omega$.

Let the source field $\mathbf{E}_{\text{source}}(\mathbf{r})$, with $\mathbf{r}$ in the exterior domain, $\mathbf{r} \in \Omega_{\text{ext}} = \mathbb{R}^3 \setminus \bar{\Omega}$, be given. Then the general scattering problem in 3D is defined by the following conditions:

1 Interior problem. The field on Ω obeys Maxwell's equations, Eq. (9).

2 Exterior problem. The field in the exterior domain is a superposition of the source and the scattered fields $\mathbf{E}_{\text{source}}$ and $\mathbf{E}_{\text{scatt}}$. Both obey Maxwell's equations.

3 Continuity of the tangential data and their normal derivative along the boundary of the computational domain is fulfilled.

4 In the case of time-harmonic fields, the Silver–Müller radiation condition for the scattered field holds true uniformly in all directions $\mathbf{r}$,

$$\lim_{|\mathbf{r}| \to \infty} |\mathbf{r}| \left[(\nabla \times \mathbf{E}_{\text{scatt}}(\mathbf{r})) \times \frac{\mathbf{r}}{|\mathbf{r}|} - i \frac{\omega}{c} \mathbf{E}_{\text{scatt}}(\mathbf{r}) \right] = 0, \tag{10}$$

where c is the speed of light in the exterior domain.

A typical application of scattering problems is the computation of light fields in single-photon source devices, see Secs. 3.2 and 5.1 and Ref. [20].

In *resonance problems* we consider Eq. (9) without sources (i.e., $\mathbf{J}_{\text{source}} = \mathbf{0}$) as an eigenvalue problem with the unknown eigenvalue ω and the unknown resonance mode, the eigenvector $\mathbf{E}$. Note that in the case of active, dispersive media with complex-valued dielectric function $\varepsilon(\mathbf{r}, \omega)$ or leaky optical cavities (open boundary conditions, e.g., Silver–Müller radiation condition), Eq. (9) is in general a non-Hermitian eigenvalue problem featuring complex resonance frequencies $\omega \in \mathbb{C}$. Here, $\mathrm{Re}\,(\omega)$ is the radial frequency of the optical field and $\mathrm{Im}\,(\omega)$ corresponds to the width of the resonance (i.e., the decay rate of the leaky optical mode) [21]. A special challenge is the treatment of the exterior domain. Either the boundary conditions on the boundary of the computational domain are explicitly known, e.g., as a magnetic or electric wall, or methods from scattering problems are applied. A typical application of resonance problems is the computation of cavity modes in semiconductor lasers. In Sec. 3.1 we outline

the self-consistent coupling of the optical resonance problem with the electronic transport problem for the simulation of QD lasers. Numerical results on cavity modes in vertical-cavity surface-emittig lasers (VCSELs) are given in Sec. 5.2.

In *mode propagation problems*, again we consider Eq. (9) without sources. This time we specialize the problem further to z-invariant problems: $\varepsilon = \varepsilon(x, y)$. We take a fixed frequency ω and look for solutions of the type $\mathbf{E}(x, y, z) = \mathbf{E}(x, y)e^{ik_z z}$ with a (unknown) phase velocity k_z. We obtain an eigenvalue problem for the waveguide mode $\mathbf{E}(x, y)$ together with its corresponding eigenvalue k_z. A typical application of mode propagation problems is the computation of propagation modes in active devices and in integrated optical setups, see Secs. 3.1 and 5.3.

2.3 Thermodynamics

Thermal effects can play an important role in opto-electronic semiconductor devices. This includes, e.g., thermal lensing and temperature-dependence of the optical gain in semiconductor lasers or self-heating in light-emitting diodes [22]. Next to an accurate modeling of thermal effects, the thermodynamic consistency of the coupled system, i.e., the consistency of the model equations with fundamental laws of (non-)equilibrium thermodynamics, is a major modeling issue.

In the framework of macroscopic device simulation, it is usually assumed that the transport and generation of heat is governed by the classical heat transport equation. In combination with the van Roosbroeck system (1), this enables the self-consistent description of several thermo-electric cross effects including Joule heating, recombination heating and the Thomson–Peltier effect [7, 23–25]. Moreover, the fully consistent thermo-electric model requires modifications in the electronic transport equations presented in Sec. 2.1. In particular, the current densities (4a) must be supplemented with an additional driving force $\sim \nabla T$ to account for the Seebeck effect. We refer to Refs. [23, 24, 26] for details.

The full thermo-opto-electronic model (see Fig. 1) is required to be consistent with fundamental principles of (non-)equilibrium thermodynamics. This comprises the consistency with the thermodynamic equilibrium (detailed balance, microscopic reversibility), the consistency with the second law of thermodynamics (non-negative entropy production rate), Onsager's reciprocal relations [27] and the preservation of conserved quantities (e.g., total charge, energy). The GENERIC (*General Equation for Non-Equilibrium Reversible-Irreversible Coupling*) formalism [28, 29] of non-equilibrium thermodynamics provides a universal approach to derive coupled and thermodynamically consistent multi-physics models for, e.g., nanophotonic semiconductor devices, where fundamental physical properties are encoded in the mathematical structure and symmetry relations of the operators and functionals driving the system's evolution [29, 30].

3 Quantum dot based light-emitting devices

In this section, two different types of nanophotonic light-emitting diodes are considered, which are both based on semiconductor quantum dots embedded in dielectric microcavities. First, in Sec. (3.1), we describe some essential ideas on a comprehensive simulation approach to QD-based micro-cavity lasers such as vertical-cavity surface-emitting lasers [31]. The model is based on a multi-species [32] description of the transport, scattering [33] and recombination dynamics of charge carriers in extended (bulk) or localized states (wetting layer (WL), QDs) coupled with the vectorial Maxwell equations (9). In contrast to these laser devices, which are based on macroscopic QD ensembles, the single-photon

sources considered in Sec. 3.2 contain only a single QD. For this case, we have developed a new hybrid quantum-classical modeling approach [34–36], which combines the building blocks of Sec. 2 with a Markovian quantum master equation [37] describing the evolution of the coupled QD-photon system.

3.1 Quantum dot lasers

Semiconductor QD lasers have been extensively studied for applications in telecommunication systems and were shown to have a variety of excellent properties that are essentially linked to the discrete energy spectrum associated with the three-dimensional carrier confinement provided by the QDs. Among others, this includes enhanced opto-electronic efficiency and differential gain, increased temperature stability, reduced threshold current and broader modulation bandwidth [3, 38].

In this section, we consider a semiconductor laser based on an ensemble of QDs embedded in an electrically pumped micro-cavity. Most prominent examples are VCSELs, but also micro-disk and micro-pillar resonators [39] belong to this type of lasers. These devices have a rather complicated geometrical structure (in comparison with conventional Fabry–Pérot lasers) and their accurate mathematical description requires a multi-dimensional simulation approach. A semi-classical description of such devices is achieved by combining the van Roosbroeck system and the vectorial (optical) Maxwell equations introduced in Secs. 2.1 and 2.2 with microscopic models for the nanostructured gain medium.

The optical field in the laser cavity is subject to the wave equation [40]

$$\nabla \times \nabla \times \mathbf{E}(\mathbf{r},t) + \frac{1}{c_0^2}\frac{\partial^2}{\partial t^2}\int_0^\infty \mathrm{d}\tau\, \varepsilon_r(\mathbf{r},t,\tau)\,\mathbf{E}(\mathbf{r},t-\tau) = -\mu_0 \frac{\partial}{\partial t}\mathbf{j}_{\mathrm{sp}}(\mathbf{r},t)\,. \tag{11}$$

The response function $\varepsilon_r(\mathbf{r},t,\tau)$ of the semiconductor depends parametrically on the slowly varying carrier densities in the active region (time scale t) and fast dephasing processes, which lead to polarization decay (time scale τ). Here, the response function describes both, the optical gain as well as cavity losses. The fluctuating current density $\mathbf{j}_{\mathrm{sp}}(\mathbf{r},t)$ induces a spontaneous polarization that is the source of spontaneous emission. The electric field is expanded in quasi-normal modes (see Sec. 2.2). For the sake of simplicity, we focus on the single-mode case $\mathbf{E}(\mathbf{r},t) = \frac{1}{2}e^{-i\omega t}A(t)\,\mathbf{E}(\mathbf{r}) + \text{c.c.}$ throughout this section, where the modal field $\mathbf{E}(\mathbf{r})$ and its complex resonance frequency ω solve the source-free Helmholtz Eq. (9)

$$\nabla \times \nabla \times \mathbf{E}(\mathbf{r}) - \frac{\omega^2}{c_0^2}\tilde{\varepsilon}_r(\mathbf{r},t,\omega)\,\mathbf{E}(\mathbf{r}) = 0 \tag{12}$$

with $\tilde{\varepsilon}_r(\mathbf{r},t,\omega) = \int_0^\infty \mathrm{d}\tau\, e^{i\omega\tau}\varepsilon_r(\mathbf{r},t,\tau)$ and outgoing wave conditions (10) on $\partial\Omega$. The evolution equation for the slowly varying mode amplitude $A(t)$ is derived under rather general conditions following Refs. [40, 41]. With an appropriate normalization of the modal field, this can be cast into the photon number equation

$$\dot{N}_{\mathrm{ph}} = 2\,\mathrm{Im}(\omega)\,N_{\mathrm{ph}} + r_{\mathrm{sp}}. \tag{13}$$

In the single mode approach outlined here, only a small additive term describing the coupling of modes under non-adiabatic conditions is omitted, which can be safely neglected in nanoresonators [40]. Expressions for the spontaneous emission r_{sp} into the given mode, which is a very small quantity in the lasers under consideration, can be found in Refs. [40–42]. Consequently, stationary lasing with a large N_{ph} requires an extremely small $\mathrm{Im}(\omega)$ that thus can be disregarded everywhere except in the photon number equation (13). Note that $\mathrm{Im}(\omega)$ contains both, positive contributions from the amplification

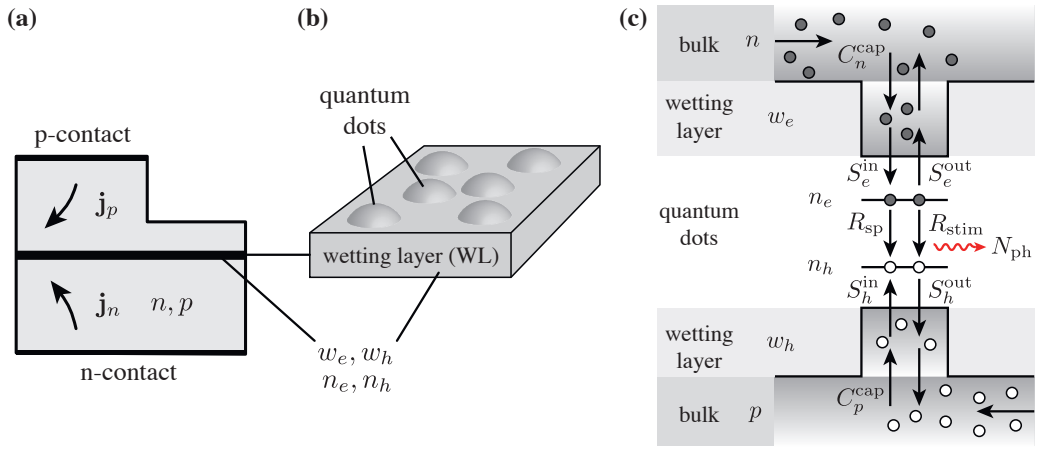

Fig. 4. (a) Sketch of a pin-diode laser structure with an embedded QD layer as optically active gain medium. **(b)** The InAs-QDs are grown on a WL acting as an additional 2D-like carrier reservoir. **(c)** Schematic illustration of scattering and recombination processes in the active region of the multi-species model. Carriers are injected from the bulk into the WL states from where they enter the QDs by Coulomb scattering. Only the QD carriers contribute to the stimulated recombination. Reprinted, with permission, from Ref. [32]. © 2016 Springer Science+Business Media.

by the QDs as well as negative contributions from optical cavity losses. In this sense, the classical threshold condition corresponds to $\mathrm{Im}\,(\omega) = 0$.

The coupling of the electronic system to the optical field equations is mainly given by the stimulated recombination rate

$$R_{\text{stim}} = \frac{\varepsilon_0}{\hbar} \int_\Omega \mathrm{d}^3 r \; \mathrm{Im}\left(\tilde{\varepsilon}_{r,\text{QD}}\left(\mathbf{r}, t, \omega\right)\right) \left|\mathbf{E}(\mathbf{r})\right|^2 N_{\text{ph}}\left(t\right), \tag{14}$$

where $\tilde{\varepsilon}_{r,\text{QD}}\left(\mathbf{r}, t, \omega\right)$ is the contribution of the QDs to the permittivity function in Eq. (12). In order to provide gain, i.e., $\mathrm{Im}\left(\tilde{\varepsilon}_{r,\text{QD}}\left(\mathbf{r}, t, \omega\right)\right) > 0$, the QDs must be sufficiently occupied with electron-hole pairs. Here, the carrier transport from the contacts of the diode to the QDs comes into play. Current flow towards the active layer is governed by the van Roosbroeck system (1) introduced in Sec. 2.1. Within the active layer, the dynamics of the electronic system is more complex. The active region has a complicated electronic density of states that features bulk scattering states, wetting layer scattering states confined in one dimension but extended in the other two dimensions, and QD states that are completely confined to individual QDs. The basic idea of a multi-species model (see Fig. 4) is to regard carriers in different types of states as different distinguishable carrier species [32]. Just as in the remaining parts of the device, the flow of bulk carriers within the active layer is also described by the van Roosbroeck system. The coupling of bulk carriers to WL and QD carriers is achieved by additional capture/ escape rates $C_{n/p}^{\text{cap}}$ added on the usual recombination rate R on the right hand side of the continuity equations (1b)–(1c). In the most simple case, quasi-equilibrium distributions can be assumed, such that these rates are effectively modeled as [6, 43, 44]

$$C_n^{\text{cap}} = \frac{n}{\tau_n}\left(1 - \frac{w_e}{N_{e,\text{WL}}^{\text{sat}}}\right)\left(1 - \exp\left(-\frac{\mu_c - \mu_c^{\text{WL}}}{k_B T}\right)\right)\Theta\left(\mathbf{r}\right),$$

where τ_n is the characteristic scattering time, μ_c^{WL} is the chemical potential of the WL electrons and $\Theta\left(\mathbf{r}\right)$ is an indicator function that is one within the active region and zero outside. The second factor describes a nonlinear reduction of the scattering rate due to state filling, where w_e is the sheet electron density in the WL and $N_{e,\text{WL}}^{\text{sat}}$ is a saturation density. An analogous expression holds for holes. In order to account for electrostatic interaction between bound and continuum carriers, the right hand side of Poisson's Eq. (1a) must be supplemented with the WL and QD carrier densities. Carrier transport within

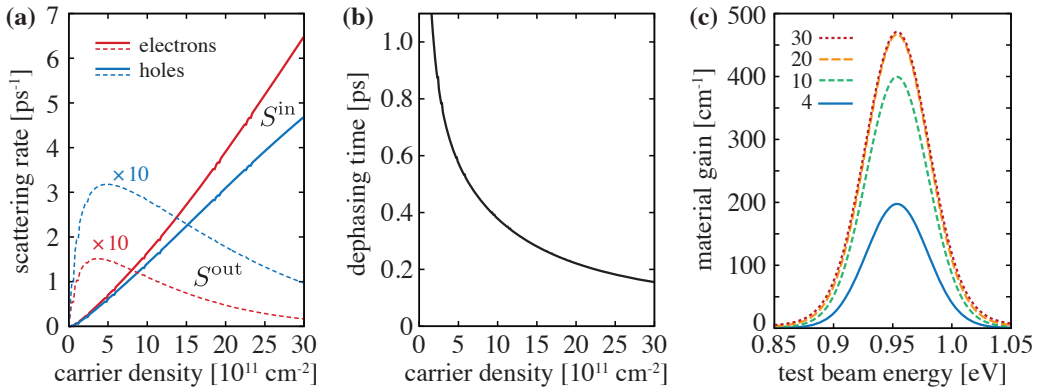

Fig. 5. (a) Calculated in (solid) and out-scattering (dahses)rates of electrons (*solid*) and holes (*dotted*) from the WL to the QD states and **(b)** dephasing time $T_2 = \Gamma_2^{-1}$ as a function of the WL sheet density ($w_e = w_h$). **(c)** Material gain spectra for WL densities $\{4, 10, 20, 30\} \times 10^{11}$ cm^{-2}. Reprinted, with permission, from Ref. [32]. © 2016 Springer Science+Business Media.

the WL is described by 2D versions of the continuity Eqs. (1b), (1c) for the WL sheet carrier densities w_e and w_h supplemented accordingly by capture/ escape terms describing the scattering to both bulk and QD states, see Fig. 4 (c). We refer to Ref. [32] for further details on the multi-species approach.

Finally, kinetic equations describing the occupation dynamics of the QD states have to be established. For conventional laser models, this implies a drastic increase of complexity, because the QDs can be occupied in several different configurations whose energies exhibit a rather wide inhomogeneous broadening. Different such scenarios have been treated in the literature [45–49]. Here we restrict ourselves to a rather simple approach based on conventional rate equations describing the dynamics of the (average) QD electron and hole occupation probabilities n_e and n_h

$$\partial_t n_e = S_e\left(n_e, n_h, w_e, w_h\right) - R_{\text{stim}}\left(n_e, n_h, w_e, w_h, N_{\text{ph}}\right) - R_{\text{sp}}\left(n_e, n_h\right), \tag{15a}$$

$$\partial_t n_h = S_h\left(n_e, n_h, w_e, w_h\right) - R_{\text{stim}}\left(n_e, n_h, w_e, w_h, N_{\text{ph}}\right) - R_{\text{sp}}\left(n_e, n_h\right), \tag{15b}$$

where $S_\nu = S_\nu^{\text{in}}\left(1 - n_\nu\right) - S_\nu^{\text{out}} n_\nu$ for $\nu \in \{e, h\}$ are the net-capture rates into the QDs and R_{stim} and R_{sp} are the total stimulated and spontaneous recombination rates. The scattering rates S_ν^{in} from the 2D (WL) and 3D (bulk) reservoirs due to Coulomb interaction can be computed microscopically using *Fermi's Golden Rule* in second order screened Born–Markov approximation, where the screening can be treated in the stationary limit using the *Lindhard formula* [33, 50, 51]. The computations involve high dimensional integrals, that can be evaluated efficiently using the quasi-Monte Carlo method [33, 52]. Assuming thermalized reservoirs (quasi-equilibrium), the in- and out-scattering rates are related by the detailed balance principle involving the respective reservoir's quasi-Fermi energy, e.g., $S_e^{\text{out}} \propto S_e^{\text{in}} \exp\left(-\mu_c^{\text{WL}}/k_B T\right)$ [46]. The characteristic dependency of the microscopically calculated Auger scattering rates (into a bound InGaAs-QD state) on the reservoir carrier density is shown in Fig. 5 (a), see Refs. [32, 33] for details. The permittivity function describing the interband polarization of the QD layer can be approximated as

$$\tilde{\varepsilon}_{r,\text{QD}}\left(\mathbf{r}, t, \omega\right) = \frac{|d_{c,v}|^2}{\varepsilon_0} N_{\text{QD}}\left(n_e + n_h - 1\right) \int_{\mathbb{R}} \mathrm{d}E \, \frac{G\left(E\right)}{i\left(E - \hbar\omega\right) + \hbar\Gamma_2\left(w_e, w_h, E\right)}, \tag{16}$$

where $d_{c,v}$ is the interband dipole moment, N_{QD} is the QD (volume) density, $G\left(E\right)$ is a Gaussian distribution function describing the inhomogeneous broadening of the QD ensemble and $\Gamma_2 = T_2^{-1}$ is the microscopically computed carrier-dependent dephasing rate [32, 53], see Fig. 5 (b). The imaginary part of Eq. (16) is the material gain (with Lorentzian line shape) that enters the stimulated recombination rate (14). Gain spectra for different reservoir carrier densities are shown in Fig. 5 (c).

3.2 Single-photon sources

Emitters of non-classical light, such as single-photon sources and sources of entangled photon pairs, are key components for many applications in the field of optical quantum communication, information processing, computing and metrology [54, 55]. Semiconductor device simulation can assist the development of engineered devices with optimized photon extraction efficiency and efficient current injection schemes. In this section, we discuss a comprehensive modeling approach for electrically driven QD-based single-photon emitting diodes. Our model is again based on the van Roosbroeck system (1) and Maxwell's wave equation (9), however, here the electro-optical coupling is described by a fully quantum mechanical model for the coupled QD-photon system. The approach is demonstrated by applications presented in Sec. 5.1 and Ref. [20].

3.2.1 Photon extraction efficiency and Purcell factor

The single-photon emission of a QD is modeled as radiation of a harmonically oscillating electric dipole polarized in the plane perpendicular to its growth axis [56]. The frequency domain electric current density $\mathbf{J}_{\mathrm{source}}$ of such a dipole with strength vector $\mathbf{j}$ at a position $\mathbf{r}_0$ is given by

$$\mathbf{J}_{\mathrm{source}}(\mathbf{r}) = \mathbf{j}\,\delta(\mathbf{r}-\mathbf{r}_0), \tag{17}$$

which enters the time-harmonic wave equation (9) as a source term. The spontaneous emission rate of the QD depends on the local density of photonic states of its specific surrounding. This is denoted as Purcell effect [57] and quantified by the dimensionless Purcell factor F_P. That is the total emitted power P_{source} of the dipole source in a structured area relative to its emission power P_{bulk} in a homogeneous environment with the same background material (with refractive inde n_b), and is calculated as follows [58]:

$$F_P = \frac{P_{\mathsf{source}}}{P_{\mathsf{bulk}}} = P_{\mathsf{source}} \left(\frac{n_b \mu_0 \omega^2}{12\pi c_0} |\mathbf{j}|^2 \right)^{-1}. \tag{18}$$

The Purcell factor is closely related to the *quality factor* $Q \propto F_P$ which characterizes the leakiness of a device. A typical way to determine the Q-factor is to calculate the corresponding resonance frequency $\omega = \mathrm{Re}\,(\omega) + i\,\mathrm{Im}\,(\omega)$ which is an eigenvalue solution to a *resonance problem*, see Sec. 2.2. With this, the Q-factor is obtained from

$$Q = -\frac{\mathrm{Re}\,(\omega)}{2\,\mathrm{Im}\,(\omega)} = \mathrm{Re}\,(\omega)\,\tau, \tag{19}$$

where τ is identified as the resonance mode lifetime.

Furthermore, one is often interested in the extraction efficiency η, i.e., in the amount of emitted light of power P_{out} that is coupled to a specific direction and numerical aperture or into a specific mode. Thus, η can be calculated as

$$\eta = \frac{P_{\mathsf{out}}}{P_{\mathsf{source}}}. \tag{20}$$

A numerical study on the optimization of geometry parameters for the maximization of the light extraction efficiency from a QD-based single-photon source is reviewed in Ref. [20].

3.2.2 Hybrid quantum-classical modeling of quantum light-emitting diodes

This section describes a comprehensive modeling approach for the device-scale simulation of QD-based electrically driven single-photon sources. In contrast to the semi-classical approach followed in

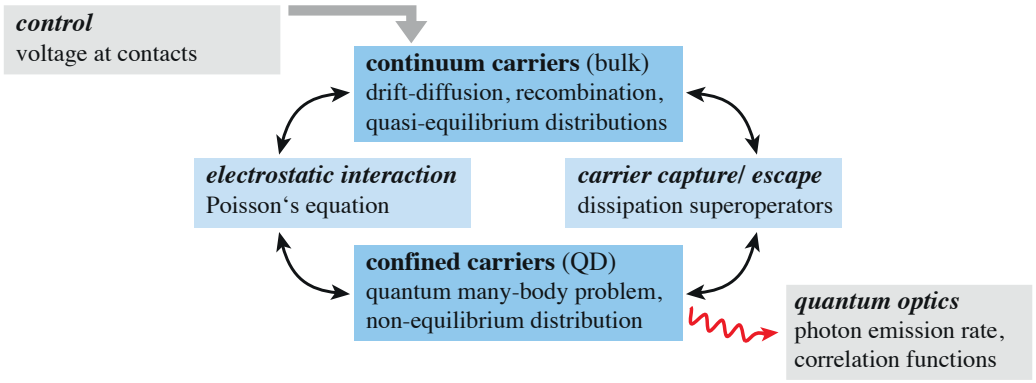

Fig. 6. Schematic representation of the hybrid quantum-classical model system (21). A quantum system described by a Lindblad-type master equation is self-consistently coupled to the semi-classical transport equations for the freely roaming continuum carriers. Both subsystems exchange charge by capture and escape of carriers and interact via their self-consistently generated electric field. Adapted, with permission, from Ref. [34]. © 2017 American Physical Society.

the laser model described in Sec. 3.1, the description of the quantum optical properties of the radiation generated by non-classical light sources requires a fully quantum mechanical modeling approach in order to access, e.g., the second-order auto-correlation function $g^{(2)}(\tau)$. This can be achieved using the second quantization formalism to describe the dynamics of the bound QD carriers coupled to the cavity photons of the optical modes supported by the resonator [38, 50]. The QD-photon system is an open quantum system that is coupled to its macroscopic environment (continuum carriers in the surrounding semiconductor, background radiation, phonons). This leads to dissipative dynamics that are conveniently described by a Markovian quantum master equation in Lindblad form for the (reduced) density matrix ρ of the open system [37].

The *hybrid quantum-classical* modeling approach developed in Refs. [34, 59] is based on the self-consistent coupling of the Lindblad master equation with the van Roosbroeck system. This allows for a multi-scale simulation of electrically driven quantum light sources, where the quantum optical properties of the QD-photon system and the spatially resolved injection current in realistic semiconductor device geometries can be calculated out of one box. The model equations read [34]

$$-\nabla\cdot\varepsilon\nabla\phi = q\left(C + p - n + Q\left(\rho\right)\right), \tag{21a}$$

$$\partial_t n - \frac{1}{q}\nabla\cdot\mathbf{j}_n = -R - S_n\left(\mu_c,\mu_v,\phi;\rho\right), \tag{21b}$$

$$\partial_t p + \frac{1}{q}\nabla\cdot\mathbf{j}_p = -R - S_p\left(\mu_c,\mu_v,\phi;\rho\right), \tag{21c}$$

$$\partial_t \rho = -\frac{i}{\hbar}\left[\mathcal{H},\rho\right] + \mathcal{D}\left(\mu_c,\mu_v,\phi\right)\rho. \tag{21d}$$

The model is based on a separation of freely roaming continuum carriers and bound carrier confined to the QD (*Born approximation*). The transport and recombination of continuum carriers is described by the van Roosbroeck system (21a)–(21c), which is extended by additional terms that constitute the coupling to the open quantum system. The coupling terms describe the bound charge density Q and the (net-)scattering rates S_n and S_p between the continuum and bound QD states. The state of the quantum system is described by the (reduced) density matrix ρ, which evolves according to the Lindblad master Eq. (21d). A schematic illustration of the model system (21) is given in Fig. 6.

The Hamiltonian $\mathcal{H}$ of the open quantum system must be chosen appropriately to the particular problem at hand. In quantum optical problems, a typical Hamiltonian takes the form

$$\mathcal{H} = \mathcal{H}_0 + \mathcal{H}_{\text{Coul}} + \mathcal{H}_{\text{LM}}. \tag{22a}$$

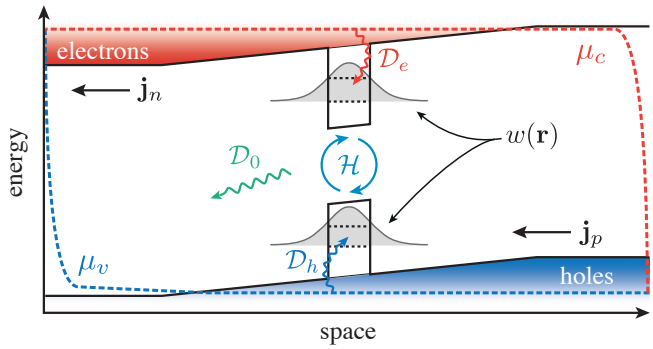

Fig. 7. Illustration of the coupling scheme and the spatial profile function $w(\mathbf{r})$ for a single QD embedded in a pin-diode structure. Adapted, with permission, from Ref. [34]. © 2017 American Physical Society.

The single-particle energies of the electrons, holes and photons are given by

$$\mathcal{H}_0 = \sum_i \varepsilon_{e,i} e_i^\dagger e_i + \sum_i \varepsilon_{h,i} h_i^\dagger h_i + \sum_i \hbar\omega_i a_i^\dagger a_i, \tag{22b}$$

where $\varepsilon_{\lambda,i}$ ($\lambda \in \{e,h\}$) denote bound QD energy levels and $\hbar\omega_i$ are the energies of the cavity photons. The fermionic creation and annihilation operators e_i and $e_i^\dagger$ (or h_i and $h_i^\dagger$) obey the usual anti-commutator relations, whereas the canonical commutator relations hold for the bosonic photon operators a_i and $a_i^\dagger$. The Coulomb interaction between the bound carriers is described by [50, 60]

$$\mathcal{H}_{\text{Coul}} = \frac{1}{2} \sum_{i,j,k,l} \left(V^{e,e}_{i,j,k,l} e_i^\dagger e_j^\dagger e_k e_l + V^{h,h}_{i,j,k,l} h_i^\dagger h_j^\dagger h_k h_l - 2V^{e,h}_{i,j,k,l} e_i^\dagger h_j^\dagger h_k e_l \right), \tag{22c}$$

where $V^{\lambda,\lambda'}_{i,j,k,l}$ are the Coulomb matrix elements. The light-matter interaction Hamiltonian (in the dipole- and rotating wave approximation) reads [38]

$$\mathcal{H}_{\text{LM}} = \sum_{i,j,k} \left(g_{i,j,k} e_i h_j a_k^\dagger + g^*_{i,j,k} a_k h_j^\dagger e_i^\dagger \right), \tag{22d}$$

where $g_{i,j,k}$ are the light-matter coupling coefficients (including also the optical selection rules). A central feature of the Hamiltonian (22) is

$$[\mathcal{H}, N] = 0, \tag{23}$$

where $N = \sum_i e_i^\dagger e_i - \sum_i h_i^\dagger h_i$ is the charge number operator. Hence, the Hamiltonian part of Eq. (21d) conserves the charge of the quantum system.

Irreversible processes (e.g., capture/ escape of carriers from continuum states to the QD, intraband carrier relaxation, spontaneous emission, pure dephasing and out-coupling of cavity photons) that arise due to the coupling of the open quantum system to its macroscopic environment are described by the dissipation superoperator

$$\mathcal{D}\left(\mu_c, \mu_v, \phi\right) \rho = \sum_{\alpha \in \mathcal{I}} \sum_{\nu,\ell} \gamma_\alpha \left(\nu, \ell; \mu_c, \mu_v, \phi\right) L_{A_\alpha(\nu,\ell)} \rho, \tag{24}$$

where γ_α is a microscopic transition rate that depends on the state (μ_c, μ_v, ϕ) of the macroscopic system, $L_A \rho = A\rho A^\dagger - \frac{1}{2}\{A^\dagger A, \rho\}$ is the Lindblad superoperator, $A_\alpha(\nu, \ell)$ is a quantum jump

operator and α labels the respective dissipative processes. The jump operators are required to obey the eigenoperator relations

$$[\mathcal{H}, A_\alpha(\nu,\ell)] = -h\nu A_\alpha(\nu,\ell), \qquad [N, A_\alpha(\nu,\ell)] = -\ell A_\alpha(\nu,\ell), \tag{25}$$

where $h\nu$ is the transition energy (with Planck's constant h) and $\ell \in \mathbb{Z}$ quantifies the amount of charge exchanged by the interaction. For each *forward* process $A_\alpha(\nu,\ell)$, the dissipation superoperator (24) involves also the corresponding *backward* process $A_\alpha^\dagger(\nu,\ell) = A(-\nu,-\ell)$. The respective forward and backward transition rates are related by a (generalized) Kubo–Martin–Schwinger condition [13] and satisfy the quantum detailed balance relation in the thermodynamic equilibrium. Due to its additive structure, the dissipation superoperator (24) can be separated as

$$\mathcal{D}\rho = \mathcal{D}_0\rho + \mathcal{D}_e\rho + \mathcal{D}_h\rho, \tag{26}$$

where the index set $\mathcal{I}$ was decomposed into disjoint subsets $\mathcal{I} = \mathcal{I}_0 \cup \mathcal{I}_e \cup \mathcal{I}_h$. This corresponds to a classification of the admitted dissipative processes with respect to their action on the charge of the quantum system. Here, $\mathcal{D}_0$ leaves the charge of the quantum system invariant (i.e., $\ell = 0$), whereas $\mathcal{D}_e$ and $\mathcal{D}_h$ describe the exchange of electrons and holes (with $\ell = \pm 1$ for one-particle exchange processes), respectively.

Finally, the quantum system couples back to the drift-diffusion system via the QD charge density Q and the scattering rates $S_{n,p}$. The charge density of a single QD can be described by the expectation value of the charge number operator

$$Q(\rho) = -w(\mathbf{r}) \operatorname{tr}(N\rho), \tag{27}$$

where $w(\mathbf{r})$ is a (normalized) spatial profile function that describes the localization of the QD carriers and phenomenologically replaces the absolute square of the many-body QD carriers wave function (see Fig. 7). The macroscopic (net-)scattering rates in Eqs. (21b)–(21c) read

$$S_n(u_w,\rho) = +w(\mathbf{r}) \operatorname{tr}(N\mathcal{D}_e(u_w)\rho), \tag{28a}$$
$$S_p(u_w,\rho) = -w(\mathbf{r}) \operatorname{tr}(N\mathcal{D}_h(u_w)\rho), \tag{28b}$$

where $u_w = (\langle\mu_c\rangle_w, \langle\mu_v\rangle_w, \langle\phi\rangle_w)$ (with $\langle\phi\rangle_w = \int \mathrm{d}^3r\, w(\mathbf{r})\,\phi(\mathbf{r},t)$ etc.) denotes the spatially averaged state of the macroscopic system in the vicinity of the QD. The scattering rates (28) summarize all microscopic charge transfer processes between the macroscopic and the quantum mechanical subsystem and are – just like the bound charge density (27) – localized according to the spatial profile function w. The microscopic scattering rates for the capture and escape of electrons $\gamma_{\alpha\in\mathcal{I}_e}$ and holes $\gamma_{\alpha\in\mathcal{I}_h}$ are obtained by microscopic calculations [33, 51, 61–63] and need to be parametrized in terms of the macroscopic potentials u_w. With the choice of (27)–(28), the hybrid system (21) inherently preserves the total charge [34].

3.2.3 Extension by Schrödinger–Poisson system

The hybrid system (21) can be extended by a self-consistent Schrödinger–Poisson system for the QD carriers to account for the quantum confined Stark effect [35, 36]. This extension is necessary to describe (bias-dependent) energy shifts of the QD excitons and the detuning of the light-matter interaction. To this end, the system (21) must be coupled to a (stationary) Schrödinger equation for each band

$$H_e^0(\phi)\,\psi_{e,i} = \varepsilon_{e,i}\psi_{e,i}, \qquad H_h^0(\phi)\,\psi_{h,i} = \varepsilon_{h,i}\psi_{h,i}, \tag{29}$$

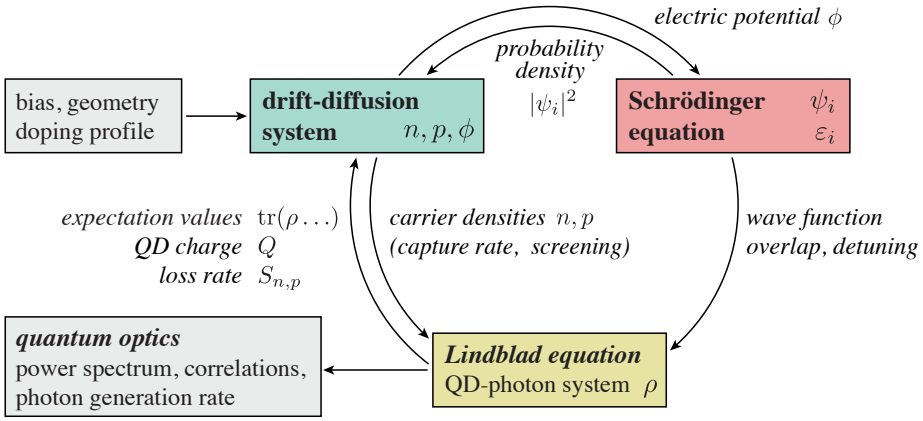

Fig. 8. Schematic representation of the extended hybrid quantum-classical modeling approach featuring a self-consistent Schrödinger–Poisson system, see Sec. 3.2.3 for details. Reprinted, with permission, from Ref. [35]. © 2019 Society of Photo-Optical Instrumentation Engineers (SPIE).

which describes the (envelope) wave functions $\psi_{\lambda,i}$ and one-particle energies $\varepsilon_{\lambda,i}$, $\lambda \in \{e, h\}$, of the QD electrons and holes in a suitably chosen confinement potential. The Schrödinger Eqs. (29) are posed on a subdomain $\Omega_0 \subseteq \Omega$ of the full computational domain and are supplemented with outgoing wave conditions on $\partial\Omega_0$. The one-particle Hamiltonians $H^0_{e,h}(\phi)$ depend on the device's internal electric potential ϕ in the vicinity of the QD, which is subject to Poisson's Eq. (21a). As a result, the (previously static) one-particle energies in the Hamiltonian (22b) are replaced by the eigenvalues of Eqs. (29), which depend dynamically on the state of the QD's macroscopic environment. Due to the dependency on the electric potential, this is in general a non-Hermitian eigenvalue problem [64], whose solutions are quasi-bound resonance modes with complex energy eigenvalues. The imaginary part of the eigenvalues describes the resonance's decay rate. Close to flat band conditions, however, the decay rate is very small and can be safely neglected such that the wave functions are normalized as $\int_{\Omega_0} \mathrm{d}^3 r \; |\psi_{\lambda,i}(\mathbf{r})|^2 = 1$ for $\lambda \in \{e, h\}$. In this extended version of the hybrid quantum-classical model, the spatial profile function $w(\mathbf{r})$ localizing the coupling terms (27)–(28) is replaced by the absolute squares of the (numerically calculated) QD wave functions $|\psi_{\lambda,i}(\mathbf{r})|^2$ [35]. With the correspondingly modified QD charge density $Q(\rho)$ entering Poisson's Eq. (21a), this yields a self-consistently coupled Schrödinger–Poisson problem. A schematic representation of the coupling scheme of the extended system is shown in Fig. 8.

The extended system (21) & (29) allows for several additional modeling refinements: Just like the single-particle energies $\varepsilon_{\lambda,i}$, also the Coulomb matrix elements $V^{\lambda,\lambda'}_{i,j,k,l}$ in Eq. (22c) depend on the state of the QD's macroscopic environment, because of (i) the variation of the wave function envelopes in the self-consistently calculated electric potential and (ii) because of screening by the continuum charge carriers in the vicinity of the QD. In Ref. [35], the plasma screening has been taken into account using the static, long wavelength limit of Lindhard's formula [50]. Finally, the light-matter coupling constants $g_{i,j,k}$ (in Eq. (22d)) and the spontaneous emission rates (corresponding $\gamma_{\alpha\in\mathcal{I}_0}(\nu, \ell)$ in $\mathcal{D}_0$) can be supplemented with the respective wave function overlap integrals.

3.2.4 Electro-optical coupling

The key process in QD-based quantum light sources is the spontaneous emission of single photons due to the recombination of bound electron-hole pairs. This is a dissipative process, that is contained in the (charge-conserving) dissipation superoperator $\mathcal{D}_0$. In the limit of very leaky, low Q resonators, the

corresponding microscopic transition rate is given by the Weisskopf–Wigner decay rate [37]

$$\gamma_{\alpha\in\mathcal{I}_0}\left(\nu,\ell=0\right)=F_P\,\frac{(2\pi)^3 n_b|d_{c,v}|^2\nu^3}{3\pi\hbar\varepsilon_0 c_0^3}\left(1+n_{\mathsf{ph}}\left(h\nu\right)\right), \tag{30}$$

where $d_{c,v}$ is the interband dipole moment, n_b is the refractive index of the background material and $n_{\mathsf{ph}}\left(h\nu\right)=\left(\exp\left(\beta h\nu\right)-1\right)^{-1}$ is the thermal photon number at the respective electronic transition energy $h\nu$. The Purcell factor F_P defined in Eq. (18) quantifies the modification of the free space decay rate due a modified local density of photonic states at the position of the QD.

3.2.5 Consistency with thermodynamic principles

The hybrid quantum-classical model system (21) has several appealing thermodynamic properties, which served as a major principle in the construction of the coupled system [13, 34]. Most strikingly, the system (21) satisfies the second law of thermodynamics, as it was shown to have a non-negative entropy production rate [34]. Moreover, it is consistent with the thermodynamic equilibrium, where the solution obeys the (quantum) detailed balance relation (microscopic reversibility) and minimizes the equilibrium grand potential

$$\Phi_{\mathsf{eq}}\left(n,p,\rho\right)=\mathcal{F}\left(n,p,\rho\right)-\mu_{\mathsf{eq}}\int_\Omega \mathrm{d}^3r\,\left(n-p-Q\left(\rho\right)\right).$$

Here, $\mathcal{F}(n,p,\rho)$ is the hybrid free energy functional that comprises both classical and quantum mechanical energy contributions [34].

The hybrid system is consistent with the GENERIC formalism (see Sec. 2.3) of non-equilibrium thermodynamics [65]. The construction is based on gradient structures for both the van Roosbroeck system (see Refs. [65, 66]) and the dissipation superoperator (24). The latter was first described in Ref. [67], where the central object is the *Onsager operator*

$$\mathbb{K}\left(\rho\right)\square=\frac{1}{2}\beta\tilde{\gamma}\left(\left[A^\dagger,\mathcal{C}_\rho^{-\beta h\nu}[A,\square]\right]+\left[A,\mathcal{C}_\rho^{\beta h\nu}[A^\dagger,\square]\right]\right), \tag{31}$$

which involves the *tilted* Kubo–Mori operator

$$\mathcal{C}_\rho^\alpha A=e^{-\frac{1}{2}\alpha}\int_0^1 \mathrm{d}s\,e^{s\alpha}\rho^s A\rho^{1-s}. \tag{32}$$

The transition rate $\tilde{\gamma}$ in Eq. (31) is connected with the scattering rates in Eq. (24) via $\gamma=\tilde{\gamma}\,\exp\left(\pm\frac{1}{2}\beta h\nu\right)$. For a quantum jump operator A obeying $[\mathcal{H},A]=-h\nu A$, the Onsager operator (31) maps the derivative of the quantum mechanical free energy contribution $\mathrm{D}_\rho\mathcal{F}=\mathcal{H}+k_BT\left(\log\rho+I\right)$ (where I is the identity operator) to the dissipation superoperator

$$\partial_t\rho|_{\mathsf{diss}}=-\mathbb{K}\left(\rho\right)\mathrm{D}_\rho\mathcal{F}=\tilde{\gamma}\left(e^{\frac{1}{2}\beta h\nu}L_A\rho+e^{-\frac{1}{2}\beta h\nu}L_{A^\dagger}\rho\right).$$

Within the GENERIC approach, the non-negativity of the corresponding dissipation rate is guaranteed by construction and follows immediately from the non-negativity of the Onsager operator $\mathbb{K}\left(\rho\right)\geq 0$ [67]

$$\begin{aligned}-\frac{1}{T}\frac{\mathrm{d}\mathcal{F}}{\mathrm{d}t}&=-\frac{1}{T}\mathrm{tr}\left(\mathrm{D}_\rho\mathcal{F}\,\partial_t\rho\right)=-\frac{1}{T}\mathrm{tr}\left(\mathrm{D}_\rho\mathcal{F}\left(-\frac{i}{\hbar}\left[\mathcal{H},\rho\right]-\mathbb{K}\left(\rho\right)\mathrm{D}_\rho\mathcal{F}\right)\right)\\&=+\frac{1}{T}\mathrm{tr}\left(\mathrm{D}_\rho\mathcal{F}\,\mathbb{K}\left(\rho\right)\,\mathrm{D}_\rho\mathcal{F}\right)\geq 0.\end{aligned}$$

Onsager's reciprocal relations are reflected by the self-adjointness $\mathbb{K}\left(\rho\right)=\mathbb{K}^\dagger\left(\rho\right)$. Without the gradient structure, the consistency with the second law of thermodynamics relies on *Spohn's inequality* [68].

4 Numerical methods

4.1 Numerical methods for the drift-diffusion equations

The numerical solution of the van Roosbroeck system requires a highly specialized discretization scheme, in order to preserve essential structural properties of the continuous system on the discrete level. Due to sudden jumps of the doping concentration (e.g., pn-junctions) or the material composition (heterostructures), the equations are typically stiff, such that it is highly desirable to obtain stable solutions also on rather coarse grids without additional smallness conditions. These problems have been, to a large extent, overcome by the finite volume discretization method together with the flux discretization scheme developed by Scharfetter and Gummel [69]. In this section, we outline the finite volume Scharfetter–Gummel method for the numerical solution of the van Roosbroeck system (1). Moreover, we discuss generalizations of the approach for strongly degenerate semiconductors and its application at cryogenic operation temperatures.

4.1.1 Finite volume method

In this section, we briefly sketch the finite volume method on unstructured grids using *restricted* Voronoï cells as control volumes. For a detailed introduction we refer to Ref. [70]. We assume a partition of the computational domain $\Omega = \bigcup_K \Omega_K$ into control volumes Ω_K. These control volumes are typically constructed from the dual mesh of a boundary conforming Delaunay triangulation [71], whose elements are called restricted Voronoï cells. The discretization of the continuous equations is achieved via integration over the control volumes and application of the divergence theorem. In the following, we use the electrostatic potential ϕ and the quasi-Fermi potentials $\phi_n = -\mu_c/q$, $\phi_p = -\mu_v/q$ as basic variables. In the most simple case (homogeneous material, homogeneous Neumann boundary conditions), we obtain the discrete van Roosbroeck system as [70]

$$F_{\phi_K^{(i)}} = \sum_{L\in\mathcal{N}(K)} s_{K,L} D_{K,L}^{(i)} - q\,|\Omega_K|\left(C_K + p_K^{(i)} - n_K^{(i)}\right), \tag{33a}$$

$$F_{\phi_{n,K}^{(i)}} = q\,|\Omega_K|\left(n_K^{(i)} - n_K^{(i-1)}\right) + \Delta t_i\Big(q\,|\Omega_K|\,R_K^{(i)} - \sum_{L\in\mathcal{N}(K)} s_{K,L} j_{n,K,L}^{(i)}\Big), \tag{33b}$$

$$F_{\phi_{p,K}^{(i)}} = q\,|\Omega_K|\left(p_K^{(i)} - p_K^{(i-1)}\right) + \Delta t_i\Big(q\,|\Omega_K|\,R_K^{(i)} + \sum_{L\in\mathcal{N}(K)} s_{K,L} j_{p,K,L}^{(i)}\Big). \tag{33c}$$

The discrete carrier densities are

$$n_K^{(i)} = n(\phi_K^{(i)}, \phi_{n,K}^{(i)}) = N_c \mathscr{F}(\eta_{n,K}^{(i)}), \qquad \eta_{n,K}^{(i)} = -\frac{E_c - q\phi_K^{(i)} + q\phi_{n,K}^{(i)}}{k_B T},$$

$$p_K^{(i)} = p(\phi_K^{(i)}, \phi_{p,K}^{(i)}) = N_v \mathscr{F}(\eta_{p,K}^{(i)}), \qquad \eta_{p,K}^{(i)} = +\frac{E_v - q\phi_K^{(i)} + q\phi_{p,K}^{(i)}}{k_B T},$$

with nodal values $u_K^{(i)} = u\,(\mathbf{r}_K, t_i)$, $u \in \{\phi, \phi_n, \phi_p\}$, evaluated at the K-th node $\mathbf{r}_K$ and time t_i (see Fig. 9). The discrete recombination rate reads $R_K^{(i)} = R(\phi_K^{(i)}, \phi_{n,K}^{(i)}, \phi_{p,K}^{(i)})$. The geometrical factors are the volume $|\Omega_K|$ of the K-th cell and the edge factor $s_{K,L} = |\partial\Omega_K \cap \partial\Omega_L| \,/\, \|\mathbf{r}_K - \mathbf{r}_L\|$, see Fig. 9. For time-discretization, we employ an implicit Euler method with time step $\Delta t_i = t_i - t_{i-1}$. The summation in the flux terms extends over all neighboring cells $L \in \mathcal{N}\,(K)$ adjacent to the K-th cell

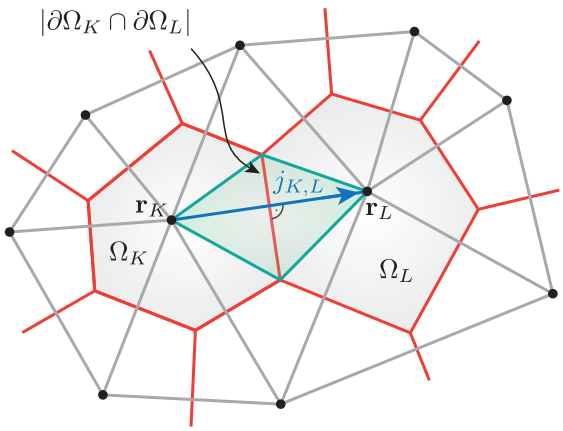

Fig. 9. Delaunay triangulation (*grey lines*) of a given point set (*black dots*) and corresponding Voronoï cells (*red lines*). The discrete flux (*blue arrow*) between the two control volumes K and L is given by the projection $j_{K,L}$ along the edge $\overline{KL}$ (see text). The flux is weighted by the edge factor $s_{K,L}$. The picture is taken from Ref. [13].

and involves the discrete flux projections

$$
\begin{aligned}
D^{(i)}_{K,L} &= (\mathbf{r}_L - \mathbf{r}_K) \cdot \mathbf{D}^{(i)} = -\varepsilon(\phi^{(i)}_L - \phi^{(i)}_K), \\
j^{(i)}_{n,K,L} &= (\mathbf{r}_L - \mathbf{r}_K) \cdot \mathbf{j}^{(i)}_n, \\
j^{(i)}_{p,K,L} &= (\mathbf{r}_L - \mathbf{r}_K) \cdot \mathbf{j}^{(i)}_p.
\end{aligned}
$$

The discretization of the carrier fluxes $j^{(i)}_{n/p,K,L}$ requires special attention and will be carried out using the Scharfetter–Gummel method outlined in Sec. 4.1.2. The linear system

$$
\mathbf{F}\left(\phi_1 \ldots \phi_N, \phi_{n,1} \ldots \phi_{n,N}, \phi_{p,1} \ldots \phi_{p,N}\right) = \mathbf{0} \tag{34}
$$

is solved using a Newton iteration method. Alternatively, a Gummel iteration [72] or combined Gummel–Newton iteration [73] can be used, which rely on decoupling, linearization and block-wise solution of the full problem.

4.1.2 Generalized Scharfetter–Gummel scheme for Fermi–Dirac statistics

The typically exponentially varying doping profiles (and therefore also carrier densities) in semiconductor devices lead to numerical instabilities when using the standard finite difference discretization. In particular, the naive discretization approach results in spurious oscillations and may cause unphysical results such as negative carrier densities [70, 74]. A robust discretization scheme for the drift-diffusion current was introduced by Scharfetter and Gummel [69], who explicitly solved the current density expressions (4b) as a separate differential equation along the edge $\overline{KL}$ between two adjacent nodes of the mesh (we drop the time step index)

$$
\frac{q\left(\phi_L - \phi_K\right)}{k_B T} = \int_{n_K}^{n_L} \mathrm{d}n \, \frac{g\left(n/N_c\right)}{\frac{j_{n,K,L}}{qM_n(\phi_L - \phi_K)} + n}. \tag{35}
$$

Assuming a constant discrete flux $j_{n,K,L}$, the integral (35) can be carried out analytically in the case of Maxwell–Boltzmann statistics ($g \equiv 1$) , leading to a discrete current formula

$$
j_{n,K,L} = M_n k_B T \left(n_L B\left(\frac{q\left(\phi_L - \phi_K\right)}{k_B T}\right) - n_K B\left(-\frac{q\left(\phi_L - \phi_K\right)}{k_B T}\right)\right). \tag{36}
$$

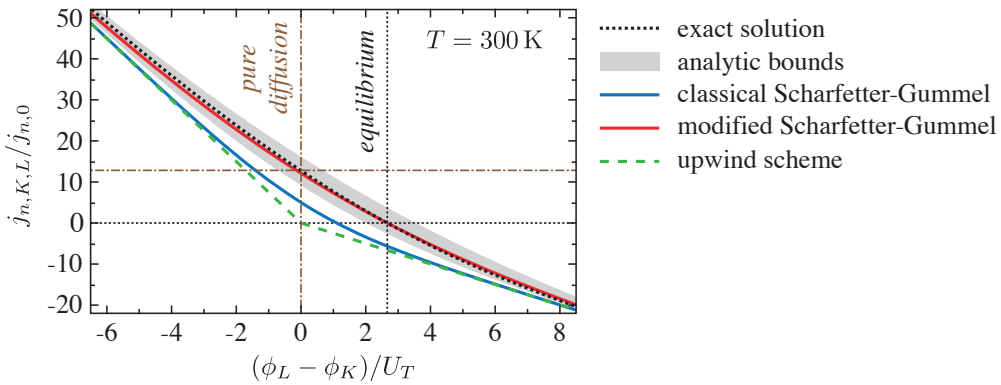

Fig. 10. Comparison of the classical and the modified Scharfetter–Gummel schemes (36) and (37) with a numerically exact solution of Eq. (35). The nodal carrier densities are $n_K = 1 \times 10^{18}\,\mathrm{cm}^{-3}$ and $n_L = 3 \times 10^{18}\,\mathrm{cm}^{-3}$. GaAs material parameters are taken from Ref. [17]. The current density projection is scaled with $j_{n,0} = M_n k_B T N_c$. The picture is taken from Ref. [13].

The exponential terms in the Bernoulli function $B(x) = x/(e^x - 1)$ reflect the characteristics of the doping profile and allow for numerically stable calculations. The so-called *Scharfetter–Gummel scheme* (36) smoothly interpolates between the central difference scheme for diffusive currents and the upwind scheme for convective flows. With the advent of the Scharfetter–Gummel discretization it became possible to accurately deal with the stiff solutions of the van Roosbroeck system on coarse grids such that practically relevant devices could be studied with a reasonable computational effort [75]. With some modifications, the method is used in many TCAD simulation tools [76, 77].

In the case of degenerate carrier statistics, the classical Scharfetter–Gummel scheme (36) breaks down and generalizations of the scheme are required. This is important, e.g., in semiconductor lasers operating at high carrier densities, organic semiconductors with Gaussian quasi-bands [78] or quantum light emitting diodes operating at extremely low temperatures [79, 80]. For weakly degenerate semiconductors following the Blakemore approximation [81], an exact generalization of the Scharfetter–Gummel scheme was obtained in Ref. [82], however, in the strongly degenerate case no closed solution of the problem (35) exists, such that one has to resort to approximations. We highlight the approach developed in Refs. [83, 84], which relies on averaging of the degeneracy factor $g \to g_{n,K,L}$ along the edge. This leads to

$$j_{n,K,L} = M_n k_B T g_{n,K,L} \left(n_L B\left(\frac{q(\phi_L - \phi_K)}{k_B T g_{n,K,L}} \right) - n_K B\left(-\frac{q(\phi_L - \phi_K)}{k_B T g_{n,K,L}} \right) \right) \tag{37a}$$

with

$$g_{n,K,L} = \frac{\eta_{n,L} - \eta_{n,K}}{\log\left(\mathscr{F}(\eta_{n,L})\right) - \log\left(\mathscr{F}(\eta_{n,K})\right)}. \tag{37b}$$

The modified Scharfetter–Gummel scheme (37) preserves many structural properties such as the consistency with the thermodynamic equilibrium and the drift- or diffusion dominated limits, while being highly accurate independent of the actual carrier statistics or the density of states function [84–86]. Figure 10 shows a comparison of the classical and the modified Scharfetter–Gummel schemes (36) and (37) with a numerical solution of the integral equation (35) obtained using Gauss–Kronrod quadrature [85, 87] in the strongly degenerate limit. We refer to Refs. [88–91] for other generalizations of the Scharfetter–Gummel scheme. The scheme (37) has been used for the simulation of the current flow in single-photon emitting diodes operating at cryogenic temperatures, in Ref. [34, 35] and Secs. 5.1, 5.4 and [20].

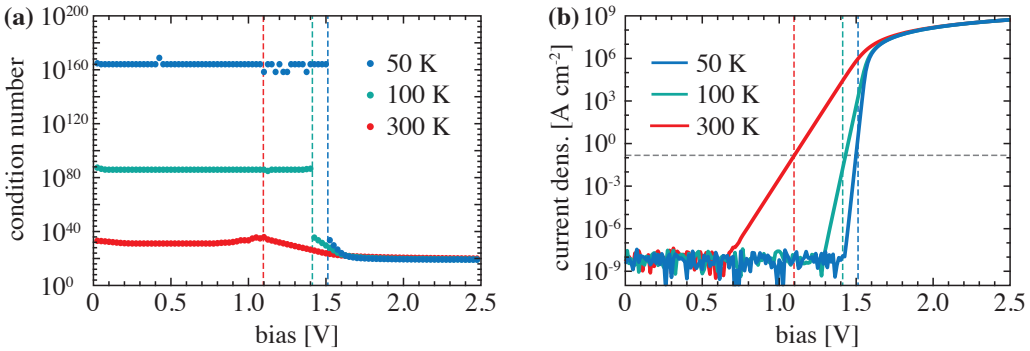

Fig. 11. (a) Condition number estimate of the Jacobian for a pin-diode problem at different temperatures and corresponding **(b)** current-voltage curves. The sudden drop of the condition number appears at the diode's threshold voltage. Adapted, with permission, from Ref. [12]. © 2016 Springer Science+Business Media.

4.1.3 Electronic transport simulation at cryogenic temperatures

At cryogenic temperatures the numerical solution of the system (33) is a challenging task and subject to serious convergence issues. Next to strong degeneration effects and sharp internal layers at pn-junctions and heterointerfaces, the major obstacle in achieving convergent solutions is the extreme depletion of minority carrier densities in the cryogenic limit. The temperature dependence of the carrier densities is given in Eq. (2) and plotted in Fig. 2 (a). As a consequence of the very low thermally activated carrier densities, the Jacobian matrix of the discrete van Roosbroeck system (33) is singular in finite precision arithmetics [12, 92, 93], such that the numerical solution of Eq. (34) is extremely sensitive to round-off errors and unfeasible using standard routines.

Indeed, the condition number estimate of the Jacobian matrix for a simple 1D-pin diode problem shown in Fig. 11 (a) reveals an exponential increase of the condition number for decreasing temperatures, as long as the diode is biased below the threshold voltage. Beyond threshold, the condition number of the cryogenic problems suddenly drops to the rather moderate value of the room temperature problem (300 K), which can be solved with standard methods. The drop of the condition number correlates with the onset of current flow as shown in Fig. 11 (b). This observation motivates the two-step temperature embedding scheme introduced in Ref. [12]. Starting from the thermodynamic equilibrium solution at an elevated temperature (e.g., room temperature), the bias is raised beyond the device's threshold voltage until flat band conditions are attained. In a second step, the temperature parameter is successively decreased until the cryogenic working point is reached. Finally, the actual computations of interest can

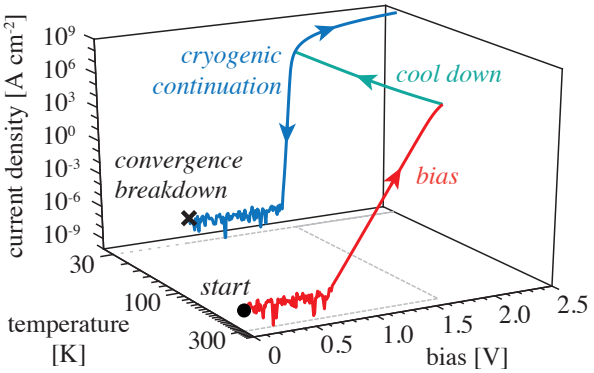

Fig. 12. Continuation scheme for transport simulation at cryogenic temperatures. After reaching flat band conditions at an elevated temperature, a solution at the cryogenic working point is obtained by successively lowering the device temperature. Reprinted, with permission, from Ref. [12]. © 2016 Springer Science+Business Media.

be carried out in the vicinity of flat band conditions. The approach is illustrated in Fig. 12 and circumvents the numerically intractable regime, by avoiding configurations with extreme carrier depletion.

We refer to Ref. [12] for a discussion of the application of the temperature embedding scheme in transport simulations in wide gap semiconductors (e.g., III-nitrides, SiC), where similar numerical problems exist.

4.2 Finite-element approach to Maxwell's equations

In this section we sketch the finite-element approach to Maxwell's equations by stating Eq. (9) in its weak form in Sec. 4.2.1 and by summarizing in Sec. 4.2.2 the finite-element expansion and specific implementations for applications discussed in Sec. 5.

4.2.1 Variational formulation

We start from the **curl**-**curl**-equation (9) for the electric field without sources, multiply with the complex conjugate of a vectorial test function $\mathbf{v}$, and integrate

$$\int_\Omega \mathrm{d}V\, \mathbf{v}^* \cdot \left(\nabla \times \mu^{-1} \nabla \times \mathbf{E}\right) - \omega^2 \int_\Omega \mathrm{d}V\, \mathbf{v}^* \cdot \varepsilon \mathbf{E} = 0. \tag{38}$$

Integration by parts yields

$$\int_\Omega \mathrm{d}V\, \left(\nabla \times \mathbf{v}^*\right) \cdot \mu^{-1} \left(\nabla \times \mathbf{E}\right) - \int_{\partial\Omega} \mathrm{d}\mathbf{A} \cdot \left(\mathbf{v}^* \times \left[\mu^{-1} \nabla \times \mathbf{E}\right]\right) - \omega^2 \int_\Omega \mathrm{d}V\, \mathbf{v}^* \cdot \varepsilon \mathbf{E} = 0. \tag{39}$$

Expressions of this type are the building blocks for the variational formulation of the Maxwell scattering problem. Let the source field data $\mathbf{E}_{\mathrm{source}}$ and $\nabla \times \mathbf{E}_{\mathrm{source}}$ at the boundary $\partial\Omega$ of the computational domain Ω be given. A typical variational form of the scattering problem reads, see e.g., Ref. [19]:

Find $\mathbf{E} \in U$:

$$a(\mathbf{v}, \mathbf{E}) = \int_{\partial\Omega} \mathrm{d}\mathbf{A} \cdot \left(\mathbf{v}^* \times \left[\left(\mu^c\right)^{-1} \nabla \times \mathbf{E}_{\mathrm{source}}\right]\right) + a_{\mathrm{ext}}\left(\mathbf{v}, \mathbf{g}\right) \tag{40}$$

$\forall \mathbf{v} \in U$ with

$$\begin{aligned}
a(\cdot,\cdot) &= a_{\mathrm{int}}(\cdot,\cdot) + a_{\mathrm{ext}}(\cdot,\cdot),\\
a_{\mathrm{int}}(\mathbf{v},\mathbf{E}) &= \int_\Omega \mathrm{d}V\, \left(\nabla \times \mathbf{v}^*\right) \cdot \mu^{-1} \left(\nabla \times \mathbf{E}\right) - \omega^2 \int_\Omega \mathrm{d}V\, \varepsilon \mathbf{v}^* \cdot \mathbf{E},\\
a_{\mathrm{ext}}(\mathbf{v},\mathbf{g}) &= \int_{\Omega_{\mathrm{ext}}} \mathrm{d}V\, \left(\nabla \times \mathbf{v}^*\right) \cdot \left(\mu^c\right)^{-1} \left(\nabla \times \mathbf{E}\right) - \omega^2 \int_{\Omega_{\mathrm{ext}}} \mathrm{d}V\, \varepsilon^c \mathbf{v}^* \cdot \mathbf{E}
\end{aligned}$$

and $\mathbf{g}$ is an arbitrary tangentially continuous function with

$$\mathbf{g}(\partial\Omega) = \mathbf{E}_{\mathrm{source}}(\partial\Omega), \qquad \mathbf{g}(\infty) = 0,$$

and

$$\left(\mu^c\right)^{-1} = \frac{1}{|J|} J^T \mu^{-1} J, \qquad \varepsilon^c = |J|\, J^{-1} \varepsilon J^{-T}.$$

The function space U ensures the tangential continuity of the vectorial fields and the existence of the first weak derivative. The exterior domain Ω_{ext} undergoes a special treatment in terms of complex continuation of the spatial coordinates to ensure an exponential decay of the scattered field. Practically this is achieved by a transformation of the material properties μ and ε, where J is the Jacobian of this transformation.

4.2.2 Patch-wise tangential continuous, polynomial approximation on unstructured grids

The finite element method (FEM) is based on a *variational formulation* of Maxwell's equations constructed from integral expressions on the computational domain, such as Eq. (40). The FEM does not use any approximation to Maxwell's equations itself, except the discretization of the geometry. However, it approximates the solution space in which one seeks a reasonable approximation to the exact solution.

The solution space of FEM is constructed by subdividing the computational domain into small, easy-to-handle patches and by providing a number of tailored polynomials on each patch for the approximation of the solution. The patches together with these local polynomials are called *finite elements*. Common examples of finite elements are triangles and rectangles in 2D and tetrahedrons and cubes in 3D. The polynomials are mostly constant, linear, quadratic and cubic expressions. These locally defined polynomial spaces are pieced together in a way that tangential continuity of the electric and magnetic field across the boundaries of neighboring patches are ensured. Once these local approximations with proper continuity conditions have been realized, these are inserted into the variational equation. Finally, this yields a linear system whose solution is a piecewise polynomial approximation of the exact solution. In summary, the two basic steps in each finite element method for Maxwell's equations are:

1 Find a variational formulation of Maxwell's equations.

2 Construct a suitable set of finite elements based on polynomials defined on local geometric patches. This transforms the variational formulation into a discrete, algebraic problem.

This concept has a number of remarkable properties:

- Complex geometrical shapes can be accurately treated, e.g., roundings can be approximated well and easily.
- The finite element mesh can easily be refined and adapted to properties of the solution, e.g., for resolving singularities at corners.
- High order approximations are available and ensure fast convergence.

In order to achieve improved solution methods for Maxwell's equations in 3D we addressed a series of numerical problems:

Hierarchic hp-adaptive finite elements

Due to the multi-scale properties of typical nanophotonic structures, conventional finite element discretizations based on tetrahedrons or hexahedrons are ineffective. We found it necessary to use mixed meshes composed of tetrahedrons, hexahedrons, prisms and pyramids. Following Ref. [94], we used an advanced setting based on hierarchical finite elements up to order 9, where the finite elements are associated to the geometric entities edge, face and cell. E.g., for prism elements, this gives the possibility to use high-order finite elements in lateral direction, where the lateral size of the element can be large, and low-order finite elements in vertical direction, where the height of the elements must be small due to the thin layers. See Fig. 15 for a typical model of a VCSEL which contains multiple length scales. We also use adaptive schemes which allow to choose between local refinement of the mesh element size h or local refinement of the polynomial order p of the finite elements, or combinations thereof [95, 96]. This results in discretizations on unstructured, locally refined meshes with polynomial order varying over the different mesh elements, so-called hp-FEM discretizations [97].

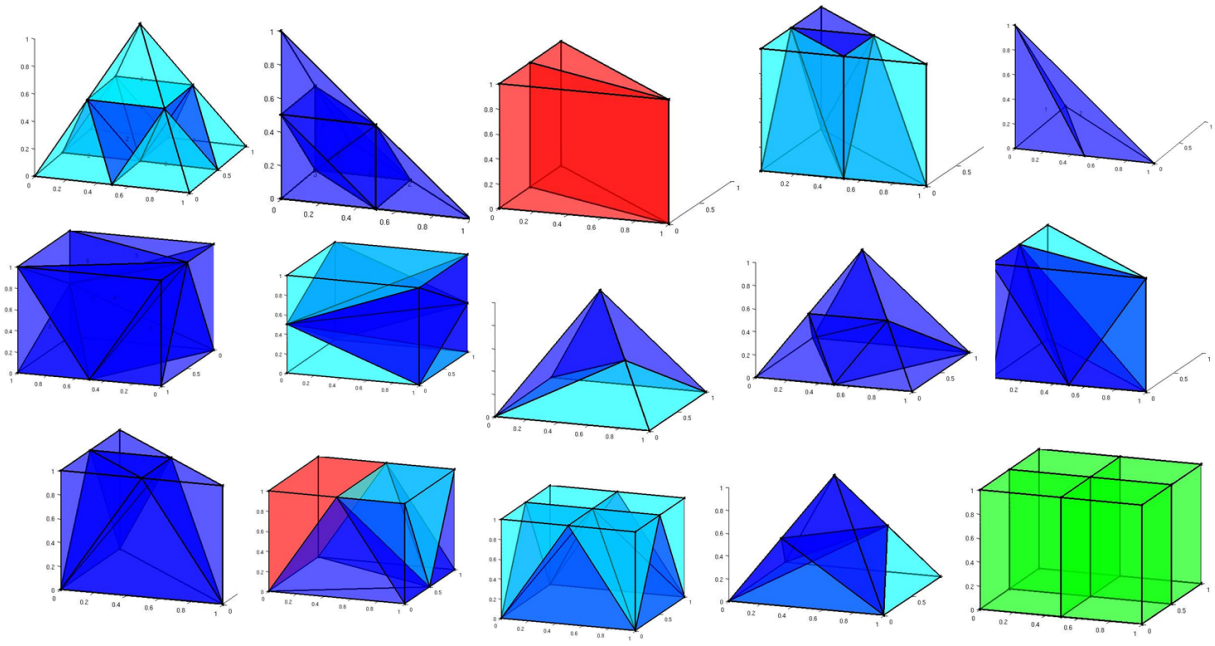

Fig. 13. Some examples of decompositions of pyramids, prisms, tetrahedrons, and hexagons. An efficient modeling of nontrivial geometries requires a careful bookkeeping of the elements and their neighborhood relations.

Modeling the geometry

For the optimization of the entire structure it is necessary to define a parameterized model of the geometry. Whereas for standard problems advanced computer-aided design (CAD) tools are available, the analysis of VCSELs and other optical structures requires a number of additional features: These are the use of mixed meshes, the modeling of isolated structures embedded into heterogeneous and unbounded exterior domains, and the treatment of exact periodic boundaries. Based on the open source kernels OpenCascade[1] and PythonOCC[2] we developed a CAD-tool which meets these needs plus the standard operations like set operations, extrusions, sweeping, revolving. Examples of mesh elements and their refinement are displayed in Fig. 13.

Specific implementations for rotationally symmetric geometries and for highly singular fields

We implemented FEM based methods in order to treat the singular fields in the vicinity of dipole sources by a subtraction-field approach. Further, this treatment has been extended to rotationally symmetric geometries, where the field radiated by the dipole can be expanded in a series of rotationally symmetric functions [56]. This approach has been applied in order to model single-photon sources [98].

5 Applications

The models and computational methods described in the previous subsections have been applied in order to simulate and to design various nanoelectronic and nanophotonic devices. This includes active devices like VCSELs [99–102], edge-emitters [8, 9, 32, 103–105], QD-based single-photon devices

[1] www.opencascade.com
[2] www.pythonocc.org

[34, 56, 79, 98, 106–111] and organic light emitting diodes [22, 112]. Also passive devices have been investigated, including metallic and dielectric nanoantennas [113–117] and -resonators [118–124], dielectric, nanostructured waveguides [95, 125, 126], plasmonic and dielectric metamaterials [127–130], and couplers for integrated optics applications [115, 131, 132]. In this section we shortly outline some of these applications.

5.1 Quantum dot single-photon sources

Single-photon sources are fundamental building blocks of future quantum communication networks [5, 133]. Self-assembled semiconductor QDs are excellent candidates for the realization of single-photon sources in the solid state as they can be easily integrated in dielectric micro-resonators and provide outstanding optical properties in terms of the suppression of multi-photon emission events and a high degree of photon indistinguishability [55, 134, 135]. The emission properties of the QD, in particular the rate of spontaneous emission [57], can be enhanced by tailoring the geometry of its surrounding structure. Moreover, the efficiencies with which the generated photons are extracted into a specific direction or coupled into an optical fiber depend strongly on the geometry of the photonic resonator [56, 106, 136].

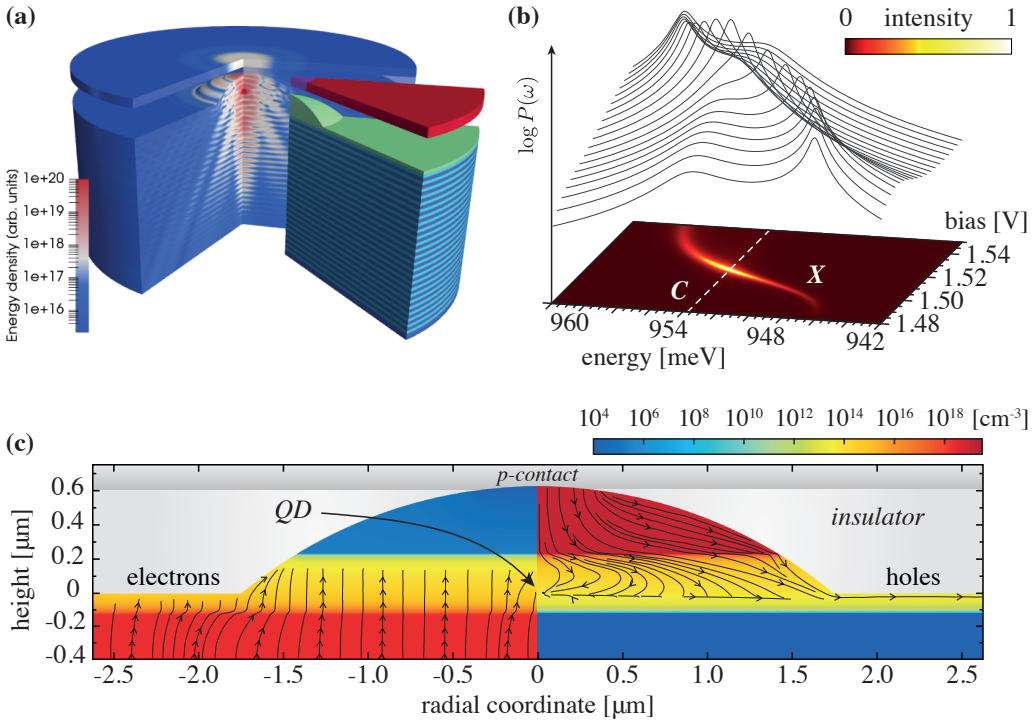

Fig. 14. Simulation of a QD-based single-photon source featuring a monolithically fabricated microlens structure at the surface. **(a)** Numerically optimized geometry (lens diameter, lens height, QD position, fiber distance) for optimal photon extraction into a single mode fiber. The energy density of the scattered electromagnetic field is color-coded. The picture is adapted with permission from Ref. [56]. © 2018 Optical Society of America (OSA). **(b)** Calculated bias dependence of the power spectrum $P(\omega)$ in a QD-based single-photon emitting diode using the hybrid modeling approach described in Secs. 3.2.2–3.2.3. The exciton line (*X*) is blue shifted due to a combination of the quantum confined Stark effect and plasma screening. The resonance with the cavity mode (*C*) appears at $U \approx 1.516$ V [35]. **(c)** 2D cross section of the spatially resolved current injection at $I = 2.75$ nA ($U = 1.49$ V DC bias) and $T = 30$ K. The geometry of the p-i-n diode structure is the same as in Fig. 14 (a). Left: Electron density n (color coded) and current density $\mathbf{j}_n$ (arrows point in the direction of electron flux). Right: Hole density p (color coded) and current density $\mathbf{j}_p$. In the low-injection regime, the scattering of continuum carriers to the QD is the dominant loss term in the transport equations, such that the QD notably contributes to current guiding. Adapted with permission from Ref. [35]. © 2019 Society of Photo-Optical Instrumentation Engineers (SPIE).

By numerical simulations of the scattering problem described in Sec. 2.2 for a harmonically oscillating electric dipole (see Sec. 3.2.1), we have optimized the geometry of the QD-based single-photon source featuring a microlens structure at the surface. The optimized geometry is shown along with the energy density of the scattered electromagnetic field in Fig. 14 (a). The geometry optimization in the high-dimensional parameter space (lens diameter, lens height, QD position, fiber distance and fiber core diameter) was carried out using a Bayesian optimization approach [56, 137]. For a detailed description of the numerical method and optimization results, we refer to Ref. [20].

In the interest of compactness and scalability, the realization of electrically driven single-photon sources is highly attractive for practical applications. We employed the hybrid quantum-classical modeling approach [34, 35, 59] described in Sec. 3.2.2 to simulate the electro-optical performance of the electrically contacted single-photon source shown in Fig. 14 (c) (same geometry as in Fig. 14 (a)). Our device-scale simulation approach allows for a comprehensive characterization of the single-photon emitting diode, as it describes the spatially resolved carrier injection into the QD, see Fig. 14 (c), along with the quantum optical features (e. g., second-order correlation function, photon generation rate, line broadening due to excitation-induced dephasing etc.) of the coupled QD-photon system. With the inclusion of the Schrödinger–Poisson system (see Sec. 3.2.3), the approach allows to describe line shifts of the exciton due to a combination of the quantum confined Stark effect and plasma screening [35], see Fig. 14 (b). A detailed description of the numerical results is given in Ref. [20].

5.2 Vertical-cavity surface-emitting lasers

VCSELs are highly miniaturized light sources with unique properties and with important applications, e.g., in optical communications [138]. The optical design of a VCSEL cavity includes finding optimum parameters for dimensions of the various cavity layers, of top and bottom distributed Bragg reflectors, as well as for apertures or further optical structures. For the design, typically the fundamental resonances of the structure can be used, as physically observable quantities like the resonance wavelength, the quality-factor, and the properties of the radiated far-field can be deduced from these. However, solving the Maxwell eigenvalue problem corresponding to Eq. (9) in this case is involved due to the different geometrical scales of the problem: thin layers of few nanometers thickness need to be resolved at a wavelength around one micron and at a total size of the device of about 10 microns in three dimensions [139], see Fig. 15 (a). In some cases, cylindrical symmetry can be used to reduce the numerical complexity, other cases do not involve such symmetries. We have demonstrated that using higher-order, adaptive finite-element methods can yield relative accuracies of the resonance wavelength of better than 10^{-8} and of the quality-factor of better than 10^{-5} [99] for a standard, rotationally symmetric VCSEL setup, following a design from the literature [139]. Further, convergence to a level of better than 10^{-5} for the resonance wavelength and 10^{-2} for the quality-factor has been demonstrated for a fully 3D setup, using elements of fourth polynomial order on a tetrahedral discretization [99]. In the same context, also coupled thermo-optical simulations have been demonstrated. These allow to quantitatively determine the impact of thermal lensing in VCSELs.

The developed methods have been applied to design single-mode VCSELs by engineering of the oxide-aperture geometry and to interpret experimental results from realized structures [100, 101]. A numerically computed electric field distribution is plotted in Fig. 15 (b). For further details on the engineering of the opto-electronic design of VCSELs we refer to Refs. [141, 142].

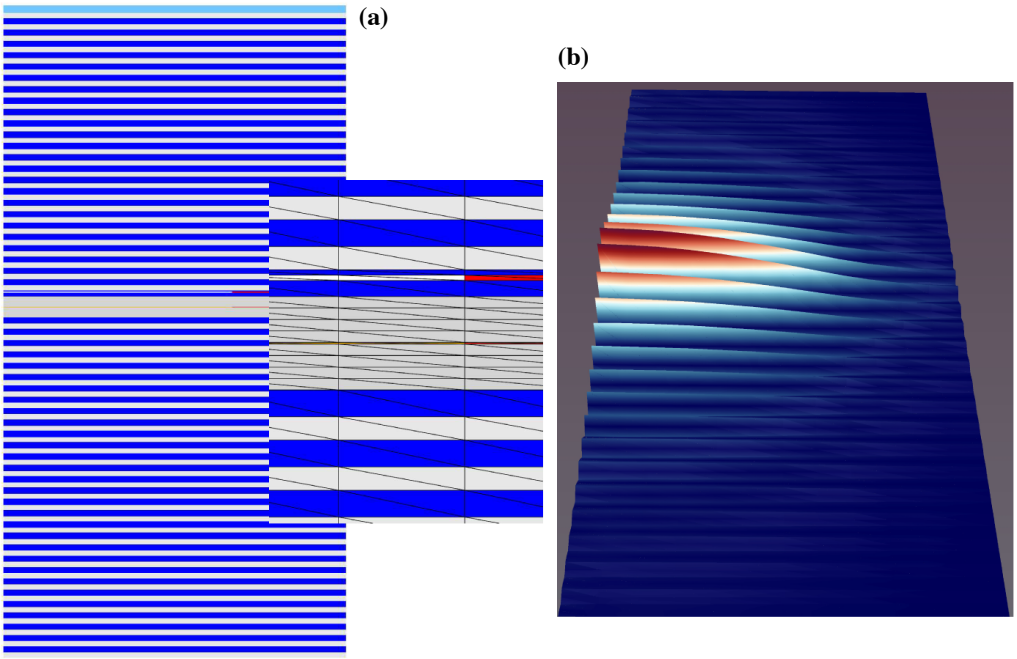

Fig. 15. (a) 2D cross section of a cylindrically symmetric VCSEL (setup as in Ref. [140]), the inset shows a detail of the finite element triangulation, including part of the 5 nm thin and 6 µm wide gain region (*orange color*). **(b)** Visualization of the computed electric field of the fundamental mode with a resonance wavelength of $\lambda = 980\,\mathrm{nm}$.

5.3 Grating couplers

By using nanostructured high refractive-index materials photonic integrated circuits can be realized with a small footprint. However, it is challenging to couple light between optical fibers and such integrated circuits. For this purpose grating couplers have been proposed to be a viable, efficient and broadband solution [143]. Optical design of grating couplers typically aims at reducing losses and thereby maximizing the coupling efficiency, which is typically defined as the optical power flux in an output waveguide directing the light from the coupler to the photonic integrated circuit divided by the optical power flux in the input optical fiber. The coupling efficiency is derived from the electromagnetic near field distribution which is obtained from simulating Eq. (9) in the form of a scattering problem. Therein the source field typically is the propagation mode in the optical waveguide, and the power flux in the output waveguide is obtained from the overlap integral between the near field distribution with the guided propagation modes of the output waveguide.

When a 2-dimensional (2D) model is sufficient, triangular meshes and 2D finite elements can be used, such that typical computation times are in the range of few seconds, which enables fast optimizations and parameter studies. However, for accurate determination of coupling efficiencies often a full 3D model is required instead. As the computational domain in this case is relatively large (several tens of micrometers in each dimension) the problem is computationally demanding. For numerically solving this problem in 3D we use higher-order finite elements on prismatoidal and tetrahedral meshes. We have shown that this allows for obtaining results with relative numerical errors of the coupling efficiency as small as about 10^{-3} for typical setups [131]. Figure 16 shows a prismatoidal mesh and visualizations of computed field distributions for a 3D grating coupler model. Also, results from a related convergence study are shown. Further, the developed methods have been used to design grating couplers capable of coupling both, fundamental and higher order modes from and to multimode fibers [132, 144]. In a related context, the methods have also been used to design and optimize coupling between integrated optical waveguides and plasmonic waveguides [115].

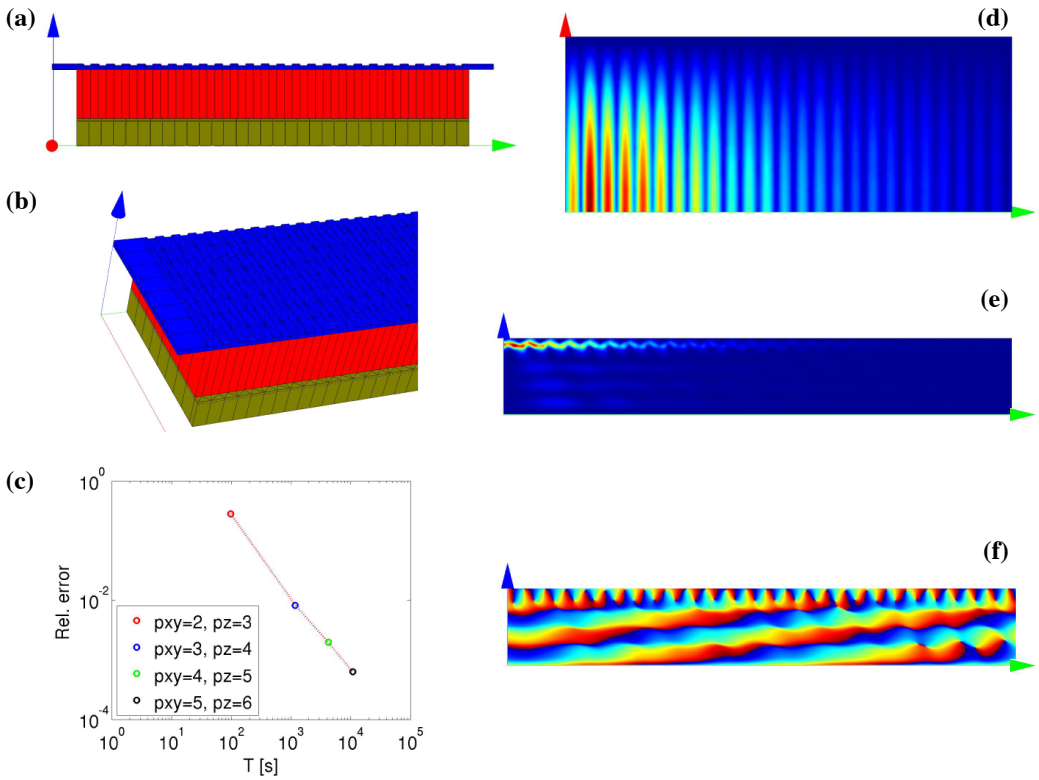

Fig. 16. (a) Visualization of a part of the mesh discretizing a 3D grating coupler model (*blue:* Si waveguide, *red:* SiO_2 buffer layer, *green:* Si substrate, coordinate axes: *red/green/blue: x/y/z*). **(b)** Detail of the mesh at oblique viewing angle. **(c)** Convergence: Relative error of the field energy in simulations with varied finite element degree (p_{xy} (p_z): polynomial order of the finite elements defined on prismatoidal mesh elements in horizontal (vertical) direction) as a function of CPU time T (specific problem setup as defined in [131]). **(d)** Visualization of the computed field intensity distribution in a cross-section through the waveguide layer. **(e)** Visualization of the computed field intensity distribution in a vertical cross section through the center of the device. **(f)** Visualization of the corresponding phase distribution of the electromagnetic field.

5.4 Efficient current injection into oxide-confined pn-diodes

Current injection into single QDs embedded in vertical pn-diodes featuring oxide apertures is essential to realize small-scale, integrable single-photon emitting diodes based on the buried stressor growth technique [145–149]. This requires efficient electrical pumping of sub-micron sized regions under pulsed excitation to achieve control over the carrier population in the central QDs. In Ref. [79] we reported on experimental and theoretical evidence for a rapid lateral spreading of the injection current after passing the oxide aperture in conventional pin-diode designs. This observation clearly contradicts the naively expected current flow indicated by the red arrows in Fig. 17 and indicates a breakdown of the current confining properties of oxidized apertures at low injection currents and cryogenic temperatures (which are the typical operation conditions of single photon emitting diodes). A theoretical analysis of the phenomenon by means of numerical simulations of the van Roosbroeck system (1) revealed the absence of carrier recombination in the intrinsic region of the diode as the primary reason for the lateral current spreading. Due to their long life time, the electrons have an enhanced diffusion length, that enables the excitation of parasitic QDs in the outer regions of the mesa, see Fig. 17. By an alternative design employing p-doping down to the oxide layer, the current spreading can be suppressed resulting in an enhanced current confinement and increased injection efficiencies [79]. For a detailed discussion of this application we refer to Ref. [150].

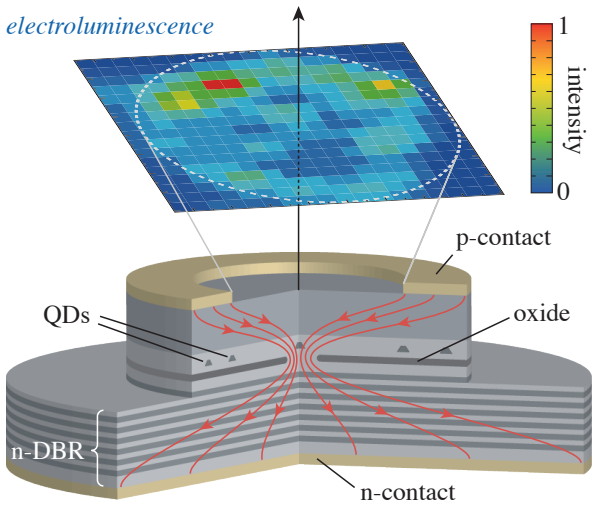

Fig. 17. Illustration of a single-photon emitting diode based on site-controlled nucleated QDs using the buried stressor approach. The electroluminescence map reveals optical activity of parasitic QDs in the outer region of the mesa, which indicates insufficient current confinement by the oxidized aperture. The naively expected current path is indicated by red arrows. The electroluminescence map is reprinted from Ref. [79].

6 Conclusion and Outlook

The computer-aided design and optimization of nanophotonic devices requires efficient numerical methods and modeling techniques. We have developed novel modeling approaches for the multi-dimensional, device-scale simulation of single-photon sources and laser diodes based on semiconductor QDs. To this end, we have coupled the optical Maxwell equations with semi-classical transport theory (van Roosbroeck system) by appropriate models for the optically active region. This includes a multi-species model for semiconductor lasers with QD active region featuring a semi-classical description of the optical response and microscopically calculated Coulomb effects (scattering, gain, dephasing). For QD-based single-photon emitting diodes, we developed a hybrid quantum-classical modeling approach, which combines the spatially resolved description of the carrier transport and optical fields with a fully quantum mechanical model for the light-matter interaction based on quantum master equations (featuring a dissipative Jaynes–Cummings model).

The application of our models to the numerical simulation of realistic devices with complex, multi-dimensional geometries and heterostructure designs asks for efficient discretization methods. For the solution of Maxwell's equations we introduced a novel hierarchic, hp-adaptive finite element approach using mixed meshes adapted to the multi-scale properties of the photonic structures. This allows for improved performance in comparison to standard finite element methods , and for numerical solutions with controlled accuracy. For the electronic transport problem , the cryogenic operation temperatures of QD-based single-photon sources impose several numerical challenges due to (i) the strong degeneration of the electron-hole plasma and (ii) the extreme depletion of the minority carrier densities. We presented a generalized finite volume Scharfetter–Gummel scheme, to accurately discretize the drift-diffusion equations for strongly degenerate semiconductors, taking the Pauli-blocking fully into account (Fermi–Dirac statistics). In addition, we developed a temperature-embedding method to overcome the stability issues of the discrete carrier transport problem at very low temperatures. The modeling approaches and numerical techniques are demonstrated on various applications, including VCSELs, grating couplers and single-photon sources.

The demonstrated advances in self-consistent modeling and multi-dimensional numerical simulation of nanophotonic devices can reveal the performance bottlenecks in new device concepts, contribute

to their understanding and help to theoretically explore their optimization potential. This makes numerical simulation an important tool, guiding important technological decisions in the development of future nanophotonic and quantum devices, such as on-chip single-photon sources and nanolasers for integrated quantum photonic circuits.

References

[1] P. Bhattacharya and Z. Mi, "Quantum-dot optoelectronic devices", Proc. IEEE **95**, 1723–1740 (2007) DOI: 10.1109/JPROC.2007.900897.

[2] P. Michler, ed., *Single Semiconductor Quantum Dots*, NanoScience and Technology (Springer, Berlin, Heidelberg, 2009), DOI: 10.1007/978-3-540-87446-1.

[3] D. Bimberg and U. W. Pohl, "Quantum dots: Promises and accomplishments", Mater. Today **14**, 388–397 (2011) DOI: 10.1016/S1369-7021(11)70183-3.

[4] P. Lodahl, S. Mahmoodian, and S. Stobbe, "Interfacing single photons and single quantum dots with photonic nanostructures", Rev. Mod. Phys. **87**, 347–400 (2015) DOI: 10.1103/revmodphys.87.347.

[5] P. Michler, ed., *Quantum Dots for Quantum Information Technologies*, Springer Series in Nano-Optics and Nanophotonics (Springer, Cham, 2017), DOI: 10.1007/978-3-319-56378-7.

[6] M. Streiff, A. Witzig, M. Pfeiffer, P. Royo, and W. Fichtner, "A comprehensive VCSEL device simulator", IEEE J. Sel. Top. Quantum Electron. **9**, 879–891 (2003) DOI: 10.1109/JSTQE.2003.818858.

[7] U Bandelow, H Gajewski, and R Hünlich, "Fabry–Perot lasers: Thermodynamics-based modeling", in *Optoelectronic Devices*, edited by J. Piprek (Springer, New York, 2005) Chap. 3, pp. 63–85, DOI: 10.1007/0-387-27256-9_3.

[8] H. Wenzel, P. Crump, H. Ekhteraei, C. Schultz, J. Pomplun, S. Burger, L. Zschiedrich, F. Schmidt, and G. Erbert, "Theoretical and experimental analysis of the lateral modes of high-power broad-area lasers", in Numerical Simulation of Optoelectronic Devices (NUSOD), 2011 11th International Conference on (IEEE, 2011), p. 143, DOI: 10.1109/nusod.2011.6041183.

[9] J. Pomplun, H. Wenzel, S. Burger, L. Zschiedrich, M. Rozova, F. Schmidt, P. Crump, H. Ekhteraei, C. M. Schultz, and G. Erbert, "Thermo-optical simulation of high-power diode lasers", Proc. SPIE **8255**, 825510 (2012) DOI: 10.1117/12.909330.

[10] W. W. van Roosbroeck, "Theory of the Flow of Electrons and Holes in Germanium and Other Semiconductors", Bell Syst. Tech. J. **29**, 560–607 (1950) DOI: 10.1002/j.1538-7305.1950.tb03653.x.

[11] S. Selberherr, *Analysis and Simulation of Semiconductor Devices* (Springer, Vienna, 1984), DOI: 10.1007/978-3-7091-8752-4.

[12] M. Kantner and T. Koprucki, "Numerical simulation of carrier transport in semiconductor devices at cryogenic temperatures", Opt. Quantum. Electron. **48**, 543 (2016) DOI: 10.1007/s11082-016-0817-2.

[13] M. Kantner, "Modeling and simulation of electrically driven quantum dot based single-photon sources: From classical device physics to open quantum systems", PhD thesis (Technical University Berlin, Berlin, 2018), DOI: 10.14279/depositonce-7516.

[14] K. Hess, *Advanced theory of semiconductor devices*, 2nd ed. (Wiley-IEEE Press, New York, 2000), DOI: 10.1109/9780470544105.

[15] C. Jacoboni, *Theory of Electron Transport in Semiconductors* (Springer, Berlin, Heidelberg, 2010), DOI: 10.1007/978-3-642-10586-9.

[16] S. M. Sze, *Physics of Semiconductor Devices*, 2nd ed. (John Wiley & Sons, New York, 1981), DOI: 10.1002/0470068329.

[17] V. Palankovski and R. Quay, *Analysis and Simulation of Heterostructure Devices*, Series in Computational Microelectronics (Springer, Vienna, 2004), DOI: 10.1007/978-3-7091-0560-3.

[18] D. Schröder, *Modelling of interface carrier transport for device simulation*, Series in Computational Microelectronics (Springer, Vienna, 1994), DOI: 10.1007/978-3-7091-6644-4.

[19] F. Schmidt, "Photonics", in *Handbook of Optoelectronic Device Modeling and Simulation: Fundamentals, Materials, Nanostructures, LEDs, and Amplifiers*, Vol. 2, edited by J. Piprek (CRC Press, Taylor & Francis Group, Boca Raton, 2017) Chap. Photonics, pp. 807–852, DOI: 10.4324/9781315152318-27.

[20] S. Rodt, P.-I. Schneider, L. Zschiedrich, T. Heindel, S. Bounouar, M. Kantner, T. Koprucki, U. Bandelow, S. Burger, and S. Reitzenstein, "Deterministic Quantum Devices for Optical Quantum Communication", in *Semiconductor*

Nanophotonics: Materials, Models, and Devices, Vol. 194, edited by M. Kneissl, A. Knorr, S. Reitzenstein, and A. Hoffmann, Springer Series in Solid-State Sciences (Springer, 2020) Chap. 8, DOI: 10.1007/978-3-030-35656-9_8.

[21] E. S. C. Ching, P. T. Leung, A. M. van den Brink, W. M. Suen, S. S. Tong, and K Young, "Quasinormal-mode expansion for waves in open systems", Rev. Mod. Phys. **70**, 1545–1554 (1998) DOI: 10.1103/revmodphys.70.1545.

[22] A. Fischer, T. Koprucki, K. Gärtner, M. L. Tietze, J. Brückner, B. Lüssem, K. Leo, A. Glitzky, and R. Scholz, "Feel the Heat: Nonlinear Electrothermal Feedback in Organic LEDs", Adv. Funct. Mater. **24**, 3367–3374 (2014) DOI: 10.1002/adfm.201303066.

[23] G. K. Wachutka, "Rigorous thermodynamic treatment of heat generation and conduction in semiconductor device modeling", IEEE Trans. Comput.-Aided Design Integr. Circuits Syst. **9**, 1141–1149 (1990) DOI: 10.1109/43.62751.

[24] U. Lindefelt, "Heat generation in semiconductor devices", J. Appl. Phys. **75**, 942–957 (1994) DOI: 10.1063/1.356450.

[25] G. Albinus, H. Gajewski, and R. Hünlich, "Thermodynamic design of energy models of semiconductor devices", Nonlinearity **15**, 367–383 (2002) DOI: 10.1088/0951-7715/15/2/307.

[26] M. Kantner, "Generalized Scharfetter–Gummel schemes for electro-thermal transport in degenerate semiconductors using the Kelvin formula for the Seebeck coefficient", J. Comput. Phys., 109091 (2019) DOI: 10.1016/j.jcp.2019.109091.

[27] L. Onsager, "Reciprocal relations in irreversible processes. I.", Phys. Rev. **37**, 405 (1931) DOI: 10.1103/PhysRev.37.405.

[28] M. Grmela and H. C. Öttinger, "Dynamics and thermodynamics of complex fluids. I. Development of a general formalism", Phys. Rev. E **56**, 6620–6632 (1997) DOI: 10.1103/PhysRevE.56.6620.

[29] A. Mielke, "Dissipative quantum mechanics using GENERIC", in *Recent Trends in Dynamical Systems*, edited by A. Johann, H.-P. Kruse, F. Rupp, and S. Schmitz, Springer Proceedings in Mathematics & Statistics 35 (Springer, Basel, 2013) Chap. 21, pp. 555–585, DOI: 10.1007/978-3-0348-0451-6_21.

[30] A. Mielke, "On thermodynamical couplings of quantum mechanics and macroscopic systems", in Mathematical Results in Quantum Mechanics, edited by P. Exner, W. König, and H. Neidhardt (2015), pp. 331–348, DOI: 10.1142/9789814618144_0029.

[31] R. Michalzik, ed., *VCSELs – Fundamentals, Technology and Applications of Vertical-Cavity Surface-Emitting Lasers*, Vol. 166, Springer Series in Optical Sciences (Springer, Berlin, Heidelberg, 2013), DOI: 10.1007/978-3-642-24986-0.

[32] T. Koprucki, A. Wilms, A. Knorr, and U. Bandelow, "Modeling of quantum dot lasers with microscopic treatment of Coulomb effects", Opt. Quantum. Electron. **42**, 777–783 (2011) DOI: 10.1007/s11082-011-9479-2.

[33] A. Wilms, P. Mathé, F. Schulze, T. Koprucki, A. Knorr, and U. Bandelow, "Influence of the carrier reservoir dimensionality on electron-electron scattering in quantum dot materials", Phys. Rev. B **88**, 235421 (2013) DOI: 10.1103/PhysRevB.88.235421.

[34] M. Kantner, M. Mittnenzweig, and T. Koprucki, "Hybrid quantum-classical modeling of quantum dot devices", Phys. Rev. B **96**, 205301 (2017) DOI: 10.1103/PhysRevB.96.205301.

[35] M. Kantner, "Hybrid modeling of quantum light emitting diodes: Self-consistent coupling of drift-diffusion, Schrödinger–Poisson and quantum master equations", Proc. SPIE **10912**, 109120U (2019) DOI: 10.1117/12.2515209.

[36] M. Kantner, T. Koprucki, H.-J. Wünsche, and U. Bandelow, "Simulation of quantum dot based single-photon sources using the Schrödinger-Poisson-Drift-Diffusion-Lindblad system", in International Conference on Simulation of Semiconductor Processes and Devices (SISPAD 2019) (IEEE, 2019), pp. 355–358, DOI: 10.1109/SISPAD.2019.8870459.

[37] H.-P. Breuer and F. Petruccione, *The Theory of Open Quantum Systems* (Oxford University Press, Oxford, 2002), DOI: 10.1093/acprof:oso/9780199213900.001.0001.

[38] W. W. Chow and F. Jahnke, "On the physics of semiconductor quantum dots for applications in lasers and quantum optics", Prog. Quantum Electron. **37**, 109–184 (2013) DOI: 10.1016/j.pquantelec.2013.04.001.

[39] S Reitzenstein and A Forchel, "Quantum dot micropillars", J. Phys. D: Appl. Phys. **43**, 033001 (2010) DOI: 10.1088/0022-3727/43/3/033001.

[40] G. A. Baraff and R. K. Smith, "Nonadiabatic semiconductor laser rate equations for the large-signal, rapid-modulation regime", Phys. Rev. A **61**, 043808, 043808 (2000) DOI: 10.1103/PhysRevA.61.043808.

[41] H. Wenzel and H.-J. Wünsche, "An equation for the amplitudes of the modes in semiconductor lasers", IEEE J. Quantum Electron. **30**, 2073–2080 (1994) DOI: 10.1109/3.309867.

[42] A. Witzig, "Modeling the Optical Processes in Semiconductor Lasers", PhD thesis (ETH Zürich, Zürich, 2002), DOI: 10.3929/ethz-a-004407405.

[43] S. Steiger, R. G. Veprek, and B. Witzigmann, "Unified simulation of transport and luminescence in optoelectronic nanostructures", J. Comput. Electron. **7**, 509–520 (2008) DOI: 10.1007/s10825-008-0261-z.

[44] M. Grupen and K. Hess, "Simulation of Carrier Transport and Nonlinearities in Quantum-Well Laser Diodes", IEEE J. Quantum Electron. **34**, 120–140 (1998) DOI: 10.1109/3.655016.

[45] W. W. Chow and S. W. Koch, “Theory of Semiconductor Quantum-Dot Laser Dynamics”, IEEE J. Quantum Electron. **41**, 495–505 (2005) DOI: 10.1109/JQE.2005.843948.

[46] K. Lüdge and E. Schöll, “Quantum-Dot Lasers–Desynchronized Nonlinear Dynamics of Electrons and Holes”, IEEE J. Quantum Electron. **45**, 1396–1403 (2009) DOI: 10.1109/jqe.2009.2028159.

[47] E. Malić, K. J. Ahn, M. J. P. Bormann, P. Hövel, E. Schöll, A. Knorr, M. Kuntz, and D. Bimberg, “Theory of relaxation oscillations in semiconductor quantum dot lasers”, Appl. Phys. Lett. **89**, 101107, 101107 (2006) DOI: 10.1063/1.2346224.

[48] N. Owschimikow, B. Herzog, B. Lingnau, K. Lüdge, A. Lenz, H. Eisele, M. Dähne, T. Niermann, M. Lehmann, A. Schliwa, A. Strittmatter, and U. W. Pohl, “Submonolayer Quantum Dots”, in *Semiconductor Nanophotonics: Materials, Models, and Devices*, Vol. 194, edited by M. Kneissl, A. Knorr, S. Reitzenstein, and A. Hoffmann, Springer Series in Solid-State Sciences (Springer, 2020) Chap. 2, DOI: 10.1007/978-3-030-35656-9_2.

[49] M. Kolarczik, F. Böhm, U. Woggon, N. Owschimikow, A. Pimenov, M. Wolfrum, A. Vladimirov, S. Meinecke, B. Lingnau, L. Jaurigue, and K. Lüdge, “Coherent and incoherent dynamics in quantum dots and nanophotonic devices”, in *Semiconductor Nanophotonics: Materials, Models, and Devices*, Vol. 194, edited by M. Kneissl, A. Knorr, S. Reitzenstein, and A. Hoffmann, Springer Series in Solid-State Sciences (Springer, 2020) Chap. 4, DOI: 10.1007/978-3-030-35656-9_4.

[50] H. Haug and S. W. Koch, *Quantum Theory of the Optical and Electronic Properties of Semiconductors*, 4th ed. (World Scientific, Singapore, 2004), DOI: 10.1142/5394.

[51] T. R. Nielsen, P. Gartner, and F. Jahnke, “Many-body theory of carrier capture and relaxation in semiconductor quantum-dot lasers”, Phys. Rev. B **69**, 235314 (2004) DOI: 10.1103/PhysRevB.69.235314.

[52] A. Wilms, D. Breddermann, and P. Mathé, “Theory of direct capture from two- and three-dimensional reservoirs to quantum dot states”, Phys. Status Solidi C **9**, 1278–1280 (2012) DOI: 10.1002/pssc.201100101.

[53] A. Wilms, “Coulomb induced interplay of localized and reservoir carriers in semiconductor quantum dots”, PhD thesis (Technical University Berlin, 2013), DOI: 10.14279/depositonce-3530.

[54] C. Santori, D. Fattal, and Y. Yamamoto, *Single-photon Devices and Applications* (Wiley, Weinheim, 2010).

[55] S. Buckley, K. Rivoire, and J. Vučković, “Engineered quantum dot single-photon sources”, Rep. Prog. Phys. **75**, 126503 (2012) DOI: 10.1088/0034-4885/75/12/126503.

[56] P.-I. Schneider, N. Srocka, S. Rodt, L. Zschiedrich, S. Reitzenstein, and S. Burger, “Numerical optimization of the extraction efficiency of a quantum-dot based single-photon emitter into a single-mode fiber”, Opt. Express **26**, 8479–8492 (2018) DOI: 10.1364/oe.26.008479.

[57] E. M. Purcell, “Spontaneous Emission Probabilities at Radio Frequencies”, Phys. Rev. **69**, 681 (1946) DOI: 10.1007/978-1-4615-1963-8_40.

[58] D. J. Griffiths, *Introduction to Electrodynamics* (Cambridge University Press, Cambridge, 2017), DOI: 10.1017/9781108333511.

[59] M. Kantner, M. Mittnenzweig, and T. Koprucki, “A hybrid quantum-classical modeling approach for electrically driven quantum light sources”, Proc. SPIE **10526**, 1052603 (2018) DOI: 10.1117/12.2289185.

[60] N. Baer, P. Gartner, and F. Jahnke, “Coulomb effects in semiconductor quantum dots”, Eur. Phys. J. B **42**, 231–237 (2004) DOI: 10.1140/epjb/e2004-00375-6.

[61] E. Malić, M. J. P. Bormann, P. Hövel, M. Kuntz, D. Bimberg, A. Knorr, and E. Schöll, “Coulomb damped relaxation oscillations in semiconductor quantum dot lasers”, IEEE J. Sel. Top. Quantum Electron. **13**, 1242–1248 (2007) DOI: 10.1109/ISLC.2006.1708081.

[62] I. Magnúsdóttir, A. V. Uskov, S. Bischoff, B. Tromborg, and J. Mørk, “One- and two-phonon capture processes in quantum dots”, J. Appl. Phys. **92**, 5982 (2002) DOI: 10.1063/1.1512694.

[63] R. Ferreira and G. Bastard, *Capture and Relaxation in Self-Assembled Semiconductor Quantum Dots*, 2053–2571 (Morgan & Claypool Publishers, San Rafael, CA, 2015), DOI: 10.1088/978-1-6817-4089-8.

[64] N. Moiseyev, *Non-Hermitian quantum mechanics* (Cambridge University Press, Cambridge, 2011), DOI: 10.1017/CBO9780511976186.

[65] M. Kantner, A. Mielke, M. Mittnenzweig, and N. Rotundo, “Mathematical modeling of semiconductors: From quantum mechanics to devices”, in *Topics in Applied Analysis and Optimisation*, edited by J. F. Rodrigues and M. Hintermüller, CIM Series in Mathematical Sciences (Springer, to appear 2020), DOI: 10.20347/WIAS.PREPRINT.2575.

[66] A. Mielke, “A gradient structure for reaction-diffusion systems and for energy-drift-diffusion systems”, Nonlinearity **24**, 1329–1346 (2011) DOI: 10.1088/0951-7715/24/4/016.

[67] M. Mittnenzweig and A. Mielke, “An Entropic Gradient Structure for Lindblad Equations and Couplings of Quantum Systems to Macroscopic Models”, J. Stat. Phys. **167**, 205–233 (2017) DOI: 10.1007/s10955-017-1756-4.

[68] H. Spohn, “Entropy production for quantum dynamical semigroups”, J. Math. Phys. **19**, 1227–1230 (1978) DOI: 10.1063/1.523789.

[69] D. L. Scharfetter and H. K. Gummel, "Large-signal analysis of a silicon Read diode oscillator", IEEE Trans. Electron Devices **16**, 64–77 (1969) DOI: 10.1109/t-ed.1969.16566.

[70] P. Farrell, N. Rotundo, D. H. Doan, M. Kantner, J. Fuhrmann, and T. Koprucki, "Drift-Diffusion Models", in *Handbook of Optoelectronic Device Modeling and Simulation: Lasers, Modulators, Photodetectors, Solar Cells, and Numerical Methods*, Vol. 2, edited by J. Piprek (CRC Press, Taylor & Francis Group, Boca Raton, 2017) Chap. 50, pp. 733–771, DOI: 10.4324/9781315152318-25.

[71] H. Si, K. Gärtner, and J. Fuhrmann, "Boundary conforming Delaunay mesh generation", Comput. Math. Math. Phys. **50**, 38–53 (2010) DOI: 10.1134/S0965542510010069.

[72] H. K. Gummel, "A self-consistent iterative scheme for one-dimensional steady state transistor calculations", IEEE Trans. Electron Devices **11**, 455–465 (1964) DOI: 10.1109/T-ED.1964.15364.

[73] H. Gajewski and K. Gärtner, "On the Iterative Solution of van Roosbroeck's Equations", J. Appl. Math. Mech. **72**, 19–28 (1992) DOI: 10.1002/zamm.19920720103.

[74] F. Brezzi, L. D. Marini, and P. Pietra, "Numerical simulation of semiconductor devices", Comput. Methods Appl. Mech. Eng. **75**, 493–514 (1989) DOI: 10.1016/0045-7825(89)90044-3.

[75] P. A. Markowich, *The stationary Semiconductor device equations*, Series in Computational Microelectronics (Springer, Vienna, 1986), DOI: 10.1007/978-3-7091-3678-2.

[76] Silvaco International, *Atlas User's Manual* (Santa Clara, CA, 2016).

[77] Synopsys, Inc., *Sentaurus Device UserGuide* (Mountain View, CA, 2010).

[78] S. L. M. van Mensfoort and R. Coehoorn, "Effect of Gaussian disorder on the voltage dependence of the current density in sandwich-type devices based on organic semiconductors", Phys. Rev. B **78**, 085207 (2008) DOI: 10.1103/PhysRevB.78.085207.

[79] M. Kantner, U. Bandelow, T. Koprucki, J.-H. Schulze, A. Strittmatter, and H.-J. Wünsche, "Efficient Current Injection Into Single Quantum Dots Through Oxide-Confined p-n-Diodes", IEEE Trans. Electron Devices **63**, 2036–2042 (2016) DOI: 10.1109/ted.2016.2538561.

[80] J. D. Cressler and H. A. Mantooth, eds., *Extreme Environment Electronics* (CRC Press, Taylor & Francis Group, Boca Raton, 2012), DOI: 10.1201/b13001.

[81] J. S. Blakemore, "Approximations for Fermi–Dirac integrals, especially the function $F_{1/2}(\eta)$ used to describe electron density in a semiconductor", Solid-State Electron. **25**, 1067–1076 (1982) DOI: 10.1016/0038-1101(82)90143-5.

[82] T. Koprucki and K. Gärtner, "Discretization scheme for drift-diffusion equations with strong diffusion enhancement", Opt. Quantum. Electron. **45**, 791–796 (2013) DOI: 10.1007/s11082-013-9673-5.

[83] M. Bessemoulin-Chatard, "A finite volume scheme for convection-diffusion equations with nonlinear diffusion derived from the Scharfetter–Gummel scheme", Numer. Math. **121**, 637–670 (2012) DOI: 10.1007/s00211-012-0448-x.

[84] T. Koprucki, N. Rotundo, P. Farrell, D. H. Doan, and J. Fuhrmann, "On thermodynamic consistency of a Scharfetter–Gummel scheme based on a modified thermal voltage for drift-diffusion equations with diffusion enhancement", Opt. Quantum. Electron. **47**, 1327–1332 (2015) DOI: 10.1007/s11082-014-0050-9.

[85] P. Farrell, M. Patriarca, J. Fuhrmann, and T. Koprucki, "Comparison of thermodynamically consistent charge carrier flux discretizations for Fermi–Dirac and Gauss–Fermi statistics", Opt. Quant. Electron. **50**, 101 (2018) DOI: 10.1007/s11082-018-1349-8.

[86] P. Farrell, T. Koprucki, and J. Fuhrmann, "Computational and Analytical Comparison of Flux Discretizations for the Semiconductor Device Equations beyond Boltzmann Statistics", J. Comput. Phys. **346**, 497–513 (2017) DOI: 10.1016/j.jcp.2017.06.023.

[87] M. Patriarca, P. Farrell, J. Fuhrmann, and T. Koprucki, "Highly accurate quadrature-based Scharfetter-Gummel schemes for charge transport in degenerate semiconductors", Comput. Phys. Commun. **235**, 40–49 (2019) DOI: 10.1016/j.cpc.2018.10.004.

[88] J. Fuhrmann, "Comparison and numerical treatment of generalised Nernst–Planck models", Comput. Phys. Commun. **196**, 166–178 (2015) DOI: 10.1016/j.cpc.2015.06.004.

[89] Z. Yu, D. Chen, L. So, and R. W. Dutton, *PISCES-2ET 2D Device Simulator*, tech. rep. (Integrated Circuits Laboratory, Stanford University, Stanford, 1994).

[90] H. Gajewski, "Analysis und Numerik von Ladungstransport in Halbleitern", Mitt. Ges. Angew. Math. Mech. **16**, 35–57 (1993).

[91] H. Gajewski and K. Gärtner, "On the discretization of van Roosbroeck's equations with magnetic field", J. Appl. Math. Mech. **76**, 247–264 (1996) DOI: 10.1002/zamm.19960760502.

[92] D. M. Richey, J. D. Cressler, and R. C. Jaeger, "Numerical simulation of SiGe HBT's at cryogenic temperatures", J. Phys. IV France **04**, C6–127–C6–32 (1994) DOI: 10.1051/jp4:1994620.

[93] S. Selberherr, "MOS device modeling at 77 K", IEEE Trans. Electron Devices **36**, 1464–1474 (1989) DOI: 10.1109/16.30960.

[94] M. Bergot and M. Duruflé, "High-order optimal edge elements for pyramids, prisms and hexahedra", J. Comput. Phys. **232**, 189–213 (2013) DOI: 10.1016/j.jcp.2012.08.005.

[95] J. Pomplun, S. Burger, L. Zschiedrich, and F. Schmidt, "Adaptive finite element method for simulation of optical nano structures", Phys. Status Solidi B **244**, 3419 (2007) DOI: 10.1002/pssb.200743192.

[96] S. Burger, L. Zschiedrich, J. Pomplun, S. Herrmann, and F. Schmidt, "Hp-finite element method for simulating light scattering from complex 3D structures", Proc. SPIE **9424**, 94240Z (2015) DOI: 10.1117/12.2085795.

[97] I. Babuška and M. R. Dorr, "Error estimates for the combined h and p versions of the finite element method", Numer. Math. **37**, 257–277 (1981) DOI: 10.1007/BF01398256.

[98] N. Srocka, A. Musiał, P.-I. Schneider, P. Mrowiński, P. Holewa, S. Burger, D. Quandt, A. Strittmatter, S. Rodt, S. Reitzenstein, and G. Sek, "Enhanced photon-extraction efficiency from InGaAs/GaAs quantum dots in deterministic photonic structures at 1.3 µm fabricated by in-situ electron-beam lithography", AIP Adv. **8**, 085205 (2018) DOI: 10.1063/1.5038137.

[99] M. Rozova, J. Pomplun, L. Zschiedrich, F. Schmidt, and S. Burger, "3D finite element simulation of optical modes in VCSELs", Proc. SPIE **8255**, 82550K (2012) DOI: 10.1117/12.906372.

[100] V. Shchukin, N. Ledentsov Jr, J. Kropp, G. Steinle, N. Ledentsov, S. Burger, and F. Schmidt, "Single-Mode Vertical Cavity Surface Emitting Laser via Oxide-Aperture-Engineering of Leakage of High-Order Transverse Modes", IEEE J. Quantum Electron. **50**, 990 (2014) DOI: 10.1109/jqe.2014.2364544.

[101] V. A. Shchukin, N. N. Ledentsov, J.-R. Kropp, G. Steinle, N. N. Ledentsov Jr., K. D. Choquette, S. Burger, and F. Schmidt, "Engineering of optical modes in vertical-cavity microresonators by aperture placement: applications to single-mode and near-field lasers", Proc. SPIE **9381**, 93810V (2015) DOI: 10.1117/12.2077012.

[102] T. Höhne, L. Zschiedrich, N. Haghighi, J. A. Lott, and S. Burger, "Validation of quasi-normal modes and of constant-flux modes for computing fundamental resonances of VCSELs", Proc. SPIE **106821**, 106821U (2018) DOI: 10.1117/12.2307200.

[103] J. Pomplun, S. Burger, F. Schmidt, A. Schliwa, D. Bimberg, A. Pietrzak, H. Wenzel, and G. Erbert, "Finite element simulation of the optical modes of semiconductor lasers", Phys. Status Solidi B **247**, 846 (2010) DOI: 10.1002/pssb.200945451.

[104] D Peschka, M Thomas, A Glitzky, R Nürnberg, K Gärtner, M Virgilio, S Guha, T. Schroeder, G Capellini, and T. Koprucki, "Modeling of edge-emitting lasers based on tensile strained germanium microstrips", IEEE Photon. J. **7**, 1–15 (2015) DOI: 10.1109/jphot.2015.2427093.

[105] D. Peschka, M. Thomas, A. Glitzky, R. Nürnberg, M. Virgilio, S. Guha, T. Schroeder, G. Capellini, and T. Koprucki, "Robustness analysis of a device concept for edge-emitting lasers based on strained germanium", Opt. Quant. Electron. **48**, 156 (2016) DOI: 10.1007/s11082-016-0394-4.

[106] M. Gschrey, A. Thoma, P. Schnauber, M. Seifried, R. Schmidt, B. Wohlfeil, L. Krüger, J.-H. Schulze, T. Heindel, S. Burger, F. Schmidt, A. Strittmatter, S. Rodt, and S. Reitzenstein, "Highly indistinguishable photons from deterministic quantum-dot microlenses utilizing three-dimensional in situ electron-beam lithography", Nat. Commun. **6**, 7662 (2015) DOI: 10.1038/ncomms8662.

[107] P. Schnauber, A. Thoma, C. V. Heine, A. Schlehahn, L. Gantz, M. Gschrey, R. Schmidt, C. Hopfmann, B. Wohlfeil, J.-H. Schulze, A. Strittmatter, T. Heindel, S. Rodt, U. Woggon, D. Gershoni, and S. Reitzenstein, "Bright Single-Photon Sources Based on Anti-Reflection Coated Deterministic Quantum Dot Microlenses", Technologies **4**, 1 (2016) DOI: 10.3390/technologies4010001.

[108] P. Schnauber, J. Schall, S. Bounouar, T. Höhne, S.-I. Park, G.-H. Ryu, T. Heindel, S. Burger, J.-D. Song, S. Rodt, and S. Reitzenstein, "Deterministic integration of quantum dots into on-chip multi-mode interference beamsplitters using in-situ electron beam lithography", Nano Lett. **18**, 2336 (2018) DOI: 10.1021/acs.nanolett.7b05218.

[109] T. Höhne, P. Schnauber, S. Rodt, S. Reitzenstein, and S. Burger, "Numerical Investigation of Light Emission from Quantum Dots Embedded into On-Chip, Low-Index-Contrast Optical Waveguides", Phys. Status Solidi B **256**, 1800437 (2018) DOI: 10.1002/pssb.201800437.

[110] K. Żołnacz, A. Musiał, N. Srocka, J. Große, M. J. Schlösinger, P.-I. Schneider, O. Kravets, M. Mikulicz, J. Olszewski, K. Poturaj, G. Wójcik, P. Mergo, K. Dybka, M. Dyrkacz, M. Dłubek, S. Rodt, S. Burger, L. Zschiedrich, G. Sęk, S. Reitzenstein, and W. Urbańczyk, "Method for direct coupling of a semiconductor quantum dot to an optical fiber for single-photon source applications", Opt. Express **27**, 26772–26785 (2019) DOI: 10.1364/OE.27.026772.

[111] P. Mrowiński, P. Schnauber, P. Gutsche, A. Kaganskiy, J. Schall, S. Burger, S. Rodt, and S. Reitzenstein, "Directional Emission of a Deterministically Fabricated Quantum Dot–Bragg Reflection Multimode Waveguide System", ACS Photonics **6**, 2231–2237 (2019) DOI: 10.1021/acsphotonics.9b00369.

[112] A. Fischer, P. Pahner, B. Lüssem, K. Leo, R. Scholz, T. Koprucki, J. Fuhrmann, K. Gärtner, and A. Glitzky, "Self-heating effects in organic semiconductor crossbar structures with small active area", Org. Electron. **13**, 2461–2468 (2012) DOI: 10.1016/j.orgel.2012.06.046.

[113] M. Richter, F. Schlosser, M. Schoth, S. Burger, F. Schmidt, A. Knorr, and S. Mukamel, "Reconstruction of the wave functions of coupled nanoscopic emitters using a coherent optical technique", Phys. Rev. B **86**, 085308 (2012) DOI: 10.1103/physrevb.86.085308.

[114] V. E. Babicheva, S. S. Vergeles, P. E. Vorobev, and S. Burger, "Localized surface plasmon modes in a system of two interacting metallic cylinders", J. Opt. Soc. Am. B **29**, 1263 (2012) DOI: 10.1364/josab.29.001263.

[115] G. Kewes, A. W. Schell, R. Henze, R. S. Schonfeld, S. Burger, K. Busch, and O. Benson, "Design and numerical optimization of an easy-to-fabricate photon-to-plasmon coupler for quantum plasmonics", Appl. Phys. Lett. **102**, 051104 (2013) DOI: 10.1063/1.4790824.

[116] A. Abass, P. Gutsche, B. Maes, C. Rockstuhl, and E. R. Martins, "Insights into directional scattering: from coupled dipoles to asymmetric dimer nanoantennas", Opt. Express **24**, 19638–19650 (2016) DOI: 10.1364/oe.24.019638.

[117] C. Becker, S. Burger, C. Barth, P. Manley, K. Jäger, D. Eisenhauer, G. Köppel, P. Chabera, J. Chen, K. Zheng, and T. Pullerits, "Nanophotonic enhanced two-photon excited photoluminescence of perovskite quantum dots", ACS Photonics **5**, 4668–4676 (2018) DOI: 10.1021/acsphotonics.8b01199.

[118] M. Karl, B. Kettner, S. Burger, F. Schmidt, H. Kalt, and M. Hetterich, "Dependencies of micro-pillar cavity quality factors calculated with finite element methods", Opt. Express **17**, 1144 (2009) DOI: 10.1364/oe.17.001144.

[119] B. Maes, J. Petráček, S. Burger, P. Kwiecien, J. Luksch, and I. Richter, "Simulations of high-Q optical nanocavities with a gradual 1D bandgap", Opt. Express **21**, 6794 (2013) DOI: 10.1364/oe.21.006794.

[120] J. R. de Lasson, L. H. Frandsen, P. Gutsche, S. Burger, O. S. Kim, O. Breinbjerg, A. Ivanskaya, F. Wang, O. Sigmund, T. Häyrynen, A. V. Lavrinenko, J. Mork, and N. Gregersen, "Benchmarking five numerical simulation techniques for computing resonance wavelengths and quality factors in photonic crystal membrane line defect cavities", Opt. Express **26**, 11366 (2018) DOI: 10.1364/oe.26.011366.

[121] G. Kewes, F. Binkowski, S. Burger, L. Zschiedrich, and O. Benson, "Heuristic Modeling of Strong Coupling in Plasmonic Resonators", ACS Photonics **5**, 4089–4097 (2018) DOI: 10.1021/acsphotonics.8b00766.

[122] L. Zschiedrich, F. Binkowski, N. Nikolay, O. Benson, G. Kewes, and S. Burger, "Riesz-projection-based theory of light-matter interaction in dispersive nanoresonators", Phys. Rev. A **98**, 043806 (2018) DOI: 10.1103/PhysRevA.98.043806.

[123] F. Binkowski, L. Zschiedrich, M. Hammerschmidt, and S. Burger, "Modal analysis for nanoplasmonics with nonlocal material properties", Phys. Rev. B **100**, 155406 (2019) DOI: 10.1103/PhysRevB.100.155406.

[124] P. Lalanne, W. Yan, A. Gras, C. Sauvan, J.-P. Hugonin, M. Besbes, G. Demésy, M. D. Truong, B. Gralak, F. Zolla, A. Nicolet, F. Binkowski, L. Zschiedrich, S. Burger, J. Zimmerling, R. Remis, P. Urbach, H. T. Liu, and T. Weiss, "Quasinormal mode solvers for resonators with dispersive materials", J. Opt. Soc. Am. A **36**, 686–704 (2019) DOI: 10.1364/JOSAA.36.000686.

[125] R. Holzlöhner, S. Burger, P. J. Roberts, and J. Pomplun, "Efficient optimization of hollow-core photonic crystal fiber design using the finite-element method", J. Europ. Opt. Soc: Rap. Comm. **1**, 06011 (2006) DOI: 10.2971/jeos.2006.06011.

[126] J. Bethge, G. Steinmeyer, S. Burger, F. Lederer, and R. Iliew, "Guiding properties of chirped photonic crystal fibers", J. Light. Technol. **27**, 1698 (2009) DOI: 10.1109/jlt.2009.2021583.

[127] P. Gutsche, R. Mäusle, and S. Burger, "Locally Enhanced and Tunable Optical Chirality in Helical Metamaterials", Photonics **3**, 60 (2016) DOI: 10.3390/photonics3040060.

[128] P. Gutsche, L. V. Poulikakos, M. Hammerschmidt, S. Burger, and F. Schmidt, "Time-harmonic optical chirality in inhomogeneous space", Proc. SPIE **9756**, 97560X (2016) DOI: 10.1117/12.2209551.

[129] D. Werdehausen, I. Staude, S. Burger, J. Petschulat, T. Scharf, T. Pertsch, and M. Decker, "Design rules for customizable optical materials based on nanocomposites", Opt. Mater. Express **8**, 3456–3469 (2018) DOI: 10.1364/OME.8.003456.

[130] D. Werdehausen, S. Burger, I. Staude, T. Pertsch, and M. Decker, "Dispersion-engineered nanocomposites enable achromatic diffractive optical elements", Optica **6**, 1031–1038 (2019) DOI: 10.1364/OPTICA.6.001031.

[131] B. Wohlfeil, S. Burger, C. Stamatiadis, J. Pomplun, F. Schmidt, L. Zimmermann, and K. Petermann, "Numerical Simulation of Grating Couplers for Mode Multiplexed Systems", Proc. SPIE **8988**, 89880K (2014) DOI: 10.1117/12.2044461.

[132] B. Wohlfeil, G. Rademacher, C. Stamatiadis, K. Voigt, L. Zimmermann, and K. Petermann, "A Two Dimensional Fiber Grating Coupler on SOI for Mode Division Multiplexing", IEEE Photon. Technol. Lett. **28**, 1241 (2016) DOI: 10.1109/lpt.2016.2514712.

[133] H. J. Kimble, "The quantum internet", Nature **453**, 1023–1030 (2008) DOI: 10.1038/nature07127.

[134] I. Aharonovich, D. Englund, and M. Toth, "Solid-state single-photon emitters", Nat. Photonics **10**, 631 (2016) DOI: 10.1038/nphoton.2016.186.

[135] N. Somaschi, V. Giesz, L. de Santis, J. C. Loredo, M. P. Almeida, G. Hornecker, S. L. Portalupi, T. Grange, C. Antón, J. Demory, C. Gómez, I. Sagnes, N. D. Lanzillotti-Kimura, A. Lemaítre, A. Auffeves, A. G. White, L. Lanco, and P. Senellart, "Near-optimal single-photon sources in the solid state", Nat. Photonics **10**, 340–345 (2016) DOI: 10.1038/nphoton.2016.23.

[136] W. L. Barnes, G. Björk, J. M. Gérard, P. Jonsson, J. A. E. Wasey, P. T. Worthing, and V. Zwiller, "Solid-state single photon sources: Light collection strategies", Eur. Phys. J. D **18**, 197–210 (2002) DOI: 10.1140/epjd/e20020024.

[137] P.-I. Schneider, X. Garcia Santiago, V. Soltwisch, M. Hammerschmidt, S. Burger, and C. Rockstuhl, "Benchmarking five global optimization approaches for nano-optical shape optimization and parameter reconstruction", ACS Photonics (2019) DOI: 10.1021/acsphotonics.9b00706.

[138] K. Iga, "Surface-emitting laser - its birth and generation of new optoelectronics field", IEEE J. Sel. Top. Quantum Electron. **6**, 1201–1215 (2000) DOI: 10.1109/2944.902168.

[139] M. Dems, I.-S. Chung, P. Nyakas, S. Bischoff, and K. Panajotov, "Numerical methods for modeling photonic-crystal VCSELs", Opt. Express **18**, 16042–16054 (2010) DOI: 10.1364/oe.18.016042.

[140] P. Bienstman, R. Baets, J. Vukusic, A. Larsson, M. J. Noble, M. Brunner, K. Gulden, P. Debernardi, L. Fratta, G. P. Bava, H. Wenzel, B. Klein, O. Conradi, R. Pregla, S. A. Riyopoulos, J.-F. P. Seurin, and S. L. Chuang, "Comparison of optical VCSEL models on the simulation of oxide-confined devices", IEEE J. Quantum Elect. **37**, 1618–1631 (2001) DOI: 10.1109/3.970909.

[141] J. A. Lott, "Vertical Cavity Surface Emitting Laser Diodes for Communication, Sensing, and Integration", in *Semiconductor Nanophotonics: Materials, Models, and Devices*, Vol. 194, edited by M. Kneissl, A. Knorr, S. Reitzenstein, and A. Hoffmann, Springer Series in Solid-State Sciences (Springer, 2020) Chap. 10, DOI: 10.1007/978-3-030-35656-9_10.

[142] P. M. Seiler, B. Tillack, and L. Zimmermann, "VCSEL-Based Silicon Photonic Interconnect Technologies", in *Semiconductor Nanophotonics: Materials, Models, and Devices*, Vol. 194, edited by M. Kneissl, A. Knorr, S. Reitzenstein, and A. Hoffmann, Springer Series in Solid-State Sciences (Springer, 2020) Chap. 11, DOI: 10.1007/978-3-030-35656-9_11.

[143] D. Taillaert, P. Bienstman, and R. Baets, "Compact efficient broadband grating coupler for silicon-on-insulator waveguides", Opt. Lett. **29**, 2749–2751 (2004) DOI: 10.1364/ol.29.002749.

[144] B. Wohlfeil, C. Stamatiadis, M. Jäger, L. Zimmermann, S. Burger, and K. Petermann, "Integrated optical fiber grating coupler on SOI for the excitation of several higher order fiber modes", in 2014 The European Conference on Optical Communication (ECOC) (2014), pp. 1–3, DOI: 10.1109/ecoc.2014.6963980.

[145] W. Unrau, D. Quandt, J.-H. Schulze, T. Heindel, T. D. Germann, O. Hitzemann, A. Strittmatter, S. Reitzenstein, U. W. Pohl, and D. Bimberg, "Electrically driven single photon source based on a site-controlled quantum dot with self-aligned current injection", Appl. Phys. Lett. **101**, 211119 (2012) DOI: 10.1063/1.4767525.

[146] A. Strittmatter, A. Holzbecher, A. Schliwa, J.-H. Schulze, D. Quandt, T. D. Germann, A. Dreismann, O. Hitzemann, E. Stock, I. A. Ostapenko, S. Rodt, W. Unrau, U. W. Pohl, A. Hoffmann, D. Bimberg, and V. A. Haisler, "Site-controlled quantum dot growth on buried oxide stressor layers", Phys. Status Solidi A **209**, 2411–2420 (2012) DOI: 10.1002/pssa.201228407.

[147] A. Strittmatter, A. Schliwa, J.-H. Schulze, T. D. Germann, A. Dreismann, O. Hitzemann, E. Stock, I. A. Ostapenko, S. Rodt, W. Unrau, U. W. Pohl, A. Hoffmann, D. Bimberg, and V. A. Haisler, "Lateral positioning of InGaAs quantum dots using a buried stressor", Appl. Phys. Lett. **100**, 093111 (2012) DOI: 10.1063/1.3691251.

[148] F. Kießling, T. Niermann, M. Lehmann, J.-H. Schulze, A. Strittmatter, A. Schliwa, and U. W. Pohl, "Strain field of a buried oxide aperture", Phys. Rev. B **91**, 075306 (2015) DOI: 10.1103/physrevb.91.075306.

[149] M. Strauß, A. Kaganskiy, R. Voigt, P. Schnauber, J.-H. Schulze, S. Rodt, A. Strittmatter, and S. Reitzenstein, "Resonance fluorescence of a site-controlled quantum dot realized by the buried-stressor growth technique", Appl. Phys. Lett. **110**, 111101 (2017) DOI: 10.1063/1.4978428.

[150] U. W. Pohl, A. Strittmatter, A. Schliwa, M. Lehmann, T. Niermann, T. Heindel, S. Reitzenstein, M. Kantner, U. Bandelow, T. Koprucki, and H.-J. Wünsche, "Stressor-Induced Site Controlof Quantum Dots for Single-Photon Sources", in *Semiconductor Nanophotonics: Materials, Models, and Devices*, Vol. 194, edited by M. Kneissl, A. Knorr, S. Reitzenstein, and A. Hoffmann, Springer Series in Solid-State Sciences (Springer, 2020) Chap. 3, DOI: 10.1007/978-3-030-35656-9_3.